

International Journal of Modern Physics A
 © World Scientific Publishing Company

Lifetime estimations from RHIC Au+Au data

Gábor Kasza

*Wigner RCP, H-1525 Budapest 114, P.O.Box 49, Hungary
 EKV KRC, H-3200 Gyöngyös, Mátrai út 36, Hungary
 Eötvös University, H-1117 Budapest, Pázmány P. s. 1/A, Hungary
 kasza.gabor@wigner.mta.hu*

Tamás Csörgő

*Wigner RCP, H-1525 Budapest 114, P.O.Box 49, Hungary
 EKV KRC, H-3200 Gyöngyös, Mátrai út 36, Hungary
 CERN, CH-1211 Geneva 23, Switzerland
 tcsorgo@cern.ch*

Received Day Month Year

Revised Day Month Year

We discuss a recently found family of exact and analytic, finite and accelerating, 1+1 dimensional solutions of perfect fluid relativistic hydrodynamics to describe the pseudorapidity densities and longitudinal HBT-radii and to estimate the lifetime parameter and the initial energy density of the expanding fireball in Au+Au collisions at RHIC with $\sqrt{s_{NN}} = 130$ GeV and 200 GeV colliding energies. From these exact solutions of relativistic hydrodynamics, we derive a simple and powerful formula to describe the pseudorapidity density distributions in high energy proton-proton and heavy ion collisions, and derive the scaling of the longitudinal HBT radius parameter as a function of the pseudorapidity density. We improve upon several oversimplifications in Bjorken's famous initial energy density estimate, and apply our results to estimate the initial energy densities of high energy reactions with data-driven pseudorapidity distributions. When compared to similar estimates at the LHC energies, our results indicate a surprising and non-monotonic dependence of the initial energy density on the energy of heavy ion collisions.

Keywords: relativistic hydrodynamics; quark-gluon plasma; longitudinal flow; rapidity distribution; pseudorapidity distribution; HBT-radii; initial energy density.

PACS numbers:

1. Introduction

Relativistic hydrodynamics of nearly perfect fluids is the current paradigm in analyzing soft particle production processes in high energy heavy ion collisions. The development of this paradigm goes back to the classic papers of Fermi from 1950,¹ Landau from 1953² and Bjorken from 1982,³ that analyzed the statistical and collective aspects of multiparticle production in high energy collisions of elementary particles and atomic nuclei.

2 *G. Kasza, T. Csörgő*

Although hydrodynamical relations in the double-differential invariant momentum distribution and in the parameters of the Bose-Einstein correlation functions of hadron-proton collisions were observed at $\sqrt{s} = 22$ GeV colliding energies as early as in 1998,⁴ relativistic hydrodynamics of nearly perfect fluids became the dominant paradigm for heavy ion collisions only after 2004, following the publication of the White Papers of the four RHIC experiments in refs. BRAHMS,⁵ PHENIX,⁶ PHOBOS⁷ and STAR.⁸ These papers summarized the results of the first four years of data-taking at Brookhaven National Laboratory's Relativistic Heavy Ion Collider (BNL's RHIC) as a circumstantial evidence for creating a nearly perfect fluid of strongly coupled quark-gluon plasma or quark matter in $\sqrt{s_{NN}} = 200$ GeV Au+Au collisions.

Recently, the STAR Collaboration significantly sharpened this result by pointing out that the fluid created in heavy ion collisions at RHIC is not only the most perfect fluid ever made by humans but also the most vortical fluid as well.⁹ Importantly, the PHENIX collaboration demonstrated that the domain of validity of the hydrodynamical paradigm extends to p + Au, d + Au and ³He + Au collisions¹⁰ and also to as low energies as $\sqrt{s_{NN}} = 19.6$ GeV.¹¹ So by 2018, the dominant paradigm of analyzing the collisions of hadron-nucleus and small-large nucleus collisions also shifted to the domain of relativistic hydrodynamics, as reviewed recently by Ref. 12. Results by the ALICE Collaboration at LHC suggested that enhanced production of multi-strange hadrons in high-multiplicity proton-proton collisions may signal the production of a strongly coupled quark-gluon plasma not only in high energy proton/deuteron/Helium+ nucleus but also in hadron-hadron collisions.¹³ These results are re-opening the door to the application of the tools of relativistic hydrodynamics in hadron-hadron collisions too, however the applicability of the hydrodynamical paradigm in these collisions is currently under intense theoretical and experimental scrutiny. Although more than 20 years passed since hydrodynamical couplings were found in the double-differential invariant momentum distribution and in the parameters of the Bose-Einstein correlation functions of hadron-proton collisions,⁴ this field is still a subject of intense debate, where the picture that protons at high colliding energies behave in several ways similarly to a small nucleus¹⁴ are gaining popularity but not yet well known.

The theory and applications of relativistic hydrodynamics to high energy collisions was reviewed and detailed recently in Ref. 15, with special attention also to the role of analytic solutions, but with a primary interest in the hydrodynamical interpretation of azimuthal oscillations in the transverse momentum spectra, and its relation to the transverse hydrodynamical expansion. In contrast, the focus of our manuscript is to gain a deeper understanding of the longitudinal expansion dynamics of high energy heavy ion and proton-proton collisions. As reviewed recently in Ref. 16, the longitudinal momentum spectra of high energy collisions can a posteriori be very well described by exact solutions of 1+1 dimensional solutions of perfect fluid hydrodynamics, the central theme of our current investigation.

Let us also stress that this manuscript is the fourth part of a manuscript series,

that is a straightforward continuation of investigations published in Refs. 17–19. The first part of this series¹⁷ gives an introductory overview of the special research area of 1+1 dimensional exact solutions of relativistic hydrodynamics, defines the notation that we also utilize in the current work, and summarizes a recently found new class of exact solutions of perfect fluid relativistic hydrodynamics in 1+1 dimensions. This new family of exact solutions, the CKCJ solution was discovered by Csörgő, Kasza, Csanád and Jiang and presented first in Ref. 16.

The first part of this manuscript series¹⁷ connects the CKCJ solution to experimentally measured quantities by evaluating the rapidity and pseudorapidity density distributions. The second part of this manuscript series¹⁸ presents exact results for the initial energy density in high energy collisions that at the same time represent an apparently fundamental correction to the famous Bjorken estimate of initial energy density³ in high energy collisions. The third part of this manuscript series,¹⁹ evaluates the Bose-Einstein correlation functions and in a Gaussian approximation it determines the so-called Hanbury Brown - Twiss or HBT-radii in the longitudinal direction from the CKCJ solution in order to determine the life-time of the fireball created in high-energy collisions.

In this work, corresponding to the fourth part of this manuscript series, we started to investigate the excitation function of the parameters of the initial state, as reconstructed with the help of the CKCJ solution.¹⁶ The results demonstrate the advantage of analytic solutions in understanding the longitudinal dynamics of fireball evolution in high energy heavy ion collisions. We follow up Refs. 17–19 by presenting a new method to evaluate the lifetime and the initial energy density of high energy heavy-ion collisions, utilizing the recently found CKCJ family of solutions^{17–19} to describe their longitudinal expansion and the corresponding measurable, the pseudorapidity density distributions. Namely, in this paper we show new fit results for Au+Au at $\sqrt{s_{NN}} = 130$ GeV and Au+Au at $\sqrt{s_{NN}} = 200$ GeV collisions at RHIC. Through these calculations we are able to estimate the acceleration and the effective temperature of the medium at freeze-out. In this paper, we utilize these results to determine the lifetime of the fireball by fitting the longitudinal HBT-radii data of Au+Au at $\sqrt{s_{NN}} = 130$ GeV and Au+Au at $\sqrt{s_{NN}} = 200$ GeV collisions, simultaneously $dN/d\eta_p$ and the slope of the transverse momentum spectra are also described. In Ref. 18 we presented a new exact formula of the initial energy density derived from our new family of perfect fluid hydrodynamic solutions. In this new formula all the unknown parameters of the freeze-out stage can be determined by fits to pseudorapidity densities and longitudinal radii, however, the dependence on the initial proper time τ_0 remains explicit. As a consequence, our new method makes it possible to describe the initial proper time dependence of the initial energy density of the thermalized fireball in high-energy heavy-ion collisions, for predominantly 1+1 dimensional expansions.

4 *G. Kasza, T. Csörgő*

2. New, exact solutions of perfect fluid hydrodynamics

The equations of relativistic perfect fluid hydrodynamics express the local conservation of entropy and four-momentum:

$$\partial_\mu(\sigma u^\mu) = 0, \quad (1)$$

$$\partial_\nu T^{\mu\nu} = 0, \quad (2)$$

where σ is the entropy density, the four velocity is denoted by u^μ and normalized as $u^\mu u_\mu = 1$, and $T^{\mu\nu}$ stands for the energy-momentum four tensor of perfect fluids:

$$T^{\mu\nu} = (\varepsilon + p)u^\mu u^\nu - pg^{\mu\nu}. \quad (3)$$

The metric tensor is $g^{\mu\nu} = \text{diag}(1, -1, -1, -1)$, the pressure is denoted by p , and the energy density by ε . The entropy density $\sigma \equiv \sigma(x)$, the energy density $\varepsilon \equiv \varepsilon(x)$, the temperature $T \equiv T(x)$, the pressure $p \equiv p(x)$, the four-velocity $u^\mu \equiv u^\mu(x)$ and the four-momentum tensor $T^{\mu\nu} \equiv T^{\mu\nu}(x)$ are fields, i.e. they are functions of the four coordinate $x \equiv x^\mu = (t, \mathbf{r}) = (t, r_x, r_y, r_z)$, but these dependencies are suppressed in our notation. The above set of equations provides five equations for six unknown fields, and it is closed by an equation of state (EoS). For a broad class of equations of state, we may assume that the energy density ε is proportional to the pressure p with a temperature dependent proportionality factor $\kappa(T)$:

$$\varepsilon = \kappa(T)p. \quad (4)$$

This class of equations of state was shown to be thermodynamically consistent in Refs. 20, 21. For the case of zero baryochemical potential, this equation of state implies a temperature dependent function for the speed of sound c_s , that can be expressed in terms of κ as follows:

$$c_s(T) = \sqrt{\frac{\partial p}{\partial \varepsilon}} = \frac{1}{\sqrt{\kappa(T)}}. \quad (5)$$

As shown in Ref. 21, the lattice QCD equation of state at $\mu_B = 0$ belongs to this class and leads to exact solutions of fireball hydrodynamics. For more details of exact hydrodynamical solutions that use the temperature dependent speed of sound from lattice QCD, for the simplest examples and details we may refer to Ref. 20, 21 and their generalizations, including Refs. 22, 23 where one can clearly see on the level of equations that a temperature independent, average speed of sound may correspond on the average to similar exact solutions. This feature is also demonstrated on Fig. 2 of Ref. 21 where it is shown that the time evolution of the temperature in the center of a three-dimensionally expanding relativistic fireball for the lattice QCD equation of state may be actually rather close to a that of a similarly three-dimensionally expanding fireball but for an average value of a temperature independent speed of sound, corresponding to $\kappa \approx 4$, corresponding to $\langle c_s(T) \rangle \approx 0.5$. We conjecture that the temperature (in)dependence of the speed of sound is not a fundamentally difficult and analytically inaccessible feature of exact solutions of relativistic fireball hydrodynamics. However, for the sake of simplicity and in order to be able to

evaluate the experimental consequences of the CKCJ exact solution of relativistic, 1+1 dimensional hydrodynamics, we utilize a temperature independent, average value for the speed of sound from now on. This step corresponds to the $\kappa(T) = \kappa$ approximation. As our goal is to describe experimental data, we take the average value of the speed of sound from a PHENIX measurement,²⁴ that corresponds to $\langle c_s(T) \rangle = 1/\sqrt{\kappa} = 0.35 \pm 0.05$. This PHENIX value of the average speed of sound corresponds to $\kappa \approx 10_{-3}^{+1}$. The result of this PHENIX measurements thus seems to be different from the average value of the speed of sound from Monte Carlo lattice QCD simulations,²⁵ that corresponds to $\kappa_{\text{IQCD}} \approx 4 \pm 1$ according to Fig. 2 of Ref. 21.

2.1. The CKCJ solution

An exact and analytic, finite and accelerating, 1+1 dimensional solution of relativistic perfect fluid hydrodynamics was recently found by Csörgő, Kasza, Csanád and Jiang (CKCJ)¹⁶ as a family of parametric curves. The thermodynamic parameters as the entropy density σ and the temperature T are functions of the longitudinal proper time τ and the space-time rapidity η_x :

$$(\tau, \eta_x) = \left(\sqrt{t^2 - r_z^2}, \frac{1}{2} \ln \left[\frac{t + r_z}{t - r_z} \right] \right). \quad (6)$$

The fluid rapidity Ω is assumed to be independent of the proper time, $\Omega(\tau, \eta_x) \equiv \Omega(\eta_x)$. The four-velocity is chosen as $u^\mu = (\cosh(\Omega), \sinh(\Omega))$, consequently the three-velocity is $v_z = \tanh(\Omega)$. The new class of CKCJ solutions¹⁶ is given in terms of parametric curves, that can be summarized as follows:

$$\eta_x(H) = \Omega(H) - H, \quad (7)$$

$$\Omega(H) = \frac{\lambda}{\sqrt{\lambda-1}\sqrt{\kappa-\lambda}} \arctan \left(\sqrt{\frac{\kappa-\lambda}{\lambda-1}} \tanh(H) \right), \quad (8)$$

$$\sigma(\tau, H) = \sigma_0 \left(\frac{\tau_0}{\tau} \right)^\lambda \mathcal{V}_\sigma(s) \left[1 + \frac{\kappa-1}{\lambda-1} \sinh^2(H) \right]^{-\frac{\lambda}{2}}, \quad (9)$$

$$T(\tau, H) = T_0 \left(\frac{\tau_0}{\tau} \right)^\frac{\lambda}{\kappa} \mathcal{T}(s) \left[1 + \frac{\kappa-1}{\lambda-1} \sinh^2(H) \right]^{-\frac{\lambda}{2\kappa}}, \quad (10)$$

$$\mathcal{T}(s) = \frac{1}{\mathcal{V}_\sigma(s)}, \quad (11)$$

$$s(\tau, H) = \left(\frac{\tau_0}{\tau} \right)^{\lambda-1} \sinh(H) \left[1 + \frac{\kappa-1}{\lambda-1} \sinh^2(H) \right]^{-\lambda/2}. \quad (12)$$

Here H is the parameter of the parametric curves that specify the CKCJ solution, λ is the acceleration parameter, $s(\tau, H)$ stands for the scale variable, and $\mathcal{V}_\sigma(s)$ is an arbitrary positive definite scaling function for the entropy density. Physically, H is the difference of the fluid rapidity and the coordinate space rapidity. The integration constants σ_0 and T_0 stand for $\sigma(\tau_0, H=0)$ and $T(\tau_0, H=0)$, where the initial proper time is denoted by τ_0 . The space-time rapidity dependence appears

6 *G. Kasza, T. Csörgő*

only through the parameter H , which is the difference of the fluid rapidity Ω and the coordinate rapidity η_x . The CKCJ solutions are limited to a cone within the forward light-cone around midrapidity. The domain of validity of these solutions in space-time rapidity is described in details in Ref. 16.

3. Observables

This section presents the results of the observables that are derived from the CKCJ solution. First we start with the derivation of the mean multiplicity. This part is detailed here as this was not discussed in the literature before. Then we discuss the pseudorapidity density and the longitudinal HBT-radii, that are the key longitudinal dynamics dependent observables to determine the lifetime parameter of the fireball. In this manuscript we do not detail the derivation of these quantities, as these were given in Refs. 18, 19 before. In the last subsection of this section, we derive a scaling relation between the longitudinal HBT radius parameter and the pseudorapidity density.

3.1. Mean multiplicity

In order to obtain the mean multiplicity $\langle N \rangle$ and the pseudorapidity density $\frac{dN}{d\eta_p}$, we follow Refs. 18, 19 and embed these 1+1 dimensional family of solutions to the 1+3 dimensional space-time. For the sake of simplicity and clarity, we also assume, that the freeze-out hypersurface is pseudo-orthogonal to the four velocity.

In this case, the average multiplicity $\langle N \rangle$ can be calculated from the phase-space distribution with integrals over the space-time and momentum-space volumes,

$$\langle N \rangle = \frac{g}{(2\pi\hbar)^3} \int d^4x \int \frac{d^3p}{p^0} p^\mu \Sigma_\mu(x) \exp\left(-\frac{p_\mu u^\mu}{T(x)} + \frac{\mu(x)}{T(x)}\right), \quad (13)$$

where $g = 2s + 1$ is the spin degeneration factor, the chemical potential is the function of the space-time coordinates and denoted by $\mu(x) \equiv \mu$, and $\Sigma_\mu(x) \equiv \Sigma_\mu$ stands for the normal vector of the freeze-out hypersurface. As we have shown in Ref. 16 this implies for the freeze-out hypersurface of the CKCJ solution, that

$$\Sigma_\mu = u_\mu \frac{\delta(\tau - \tau_f)}{\cosh(\Omega - \eta_x)}. \quad (14)$$

Thus the invariant integration over the momentum can be performed at each point on the freeze-out hypersurface, parameterized as $\tau = \tau(\eta_x)$, to find

$$\langle N \rangle = \frac{g}{(2\pi\hbar)^3} 4\pi m^2 \int d\tau d\eta_x dr_x dr_y \delta(\tau - \tau_f) \frac{\tau T}{\cosh(\Omega - \eta_x)} K_2\left(\frac{m}{T}\right) \exp\left(\frac{\mu}{T}\right), \quad (15)$$

where K_2 stands for the modified Bessel-function of the second kind and the integral measure is rewritten as $d^4x = \tau d\tau d\eta_x dr_x dr_y$. We assume, that close to the midrapidity region the temperature is approximately independent from η_x and the

transverse coordinates so it is approximately a constant freeze-out temperature T_f . Using these approximations, Eq. (15) can be simplified as:

$$\langle N \rangle = \frac{g}{(2\pi\hbar)^3} 4\pi m^2 T_f K_2\left(\frac{m}{T_f}\right) \int d\eta_x dr_x dr_y \frac{\tau_f}{\cosh(\Omega - \eta_x)} \exp\left(\frac{\mu}{T_f}\right), \quad (16)$$

where we note the suppressed coordinate-space rapidity η_x and transverse coordinate (r_x, r_y) dependence of the fugacity factor $\exp(\frac{\mu}{T_f})$. As already clear from Ref. 16, this fugacity factor contributes importantly to the shape of coordinate rapidity density and hence to the measurable (pseudo)rapidity distribution. At the end of this sub-section, we shall approximate this factor by Gaussians both in η_x and in the transverse coordinates (r_x, r_y) .

Let us also introduce V_x for the spatial volume, and V_p for the local volume of the momentum space (corresponding to particles emitted at the same coordinate position x .) Let us also denote by \bar{f} the average phase space density.

The average number of particles $\langle N \rangle$ – also referred to as the mean multiplicity – is given by these quantities in a rather trivial and straight-forward manner:

$$\langle N \rangle = \frac{g}{(2\pi\hbar)^3} \bar{f} V_x V_p, \quad (17)$$

where the average phase-space density is $\bar{f} = \exp(\bar{\mu}/T_f)$ and $\bar{\mu}$ stands for the average value of the chemical potential for the particles characterized by mass m . From Eqs. (16) and (17) one finds the formulae of the volumes of both the coordinate-space (V_x given in terms of the fugacity distribution) and of the momentum space (V_p , given in terms of the freeze-out temperature T_f and the mass m) as:

$$V_x = \int d\eta_x dr_x dr_y \frac{\tau_f}{\cosh(\Omega - \eta_x)} \exp\left(\frac{\mu(\tau_f, \eta_x, r_x, r_y) - \bar{\mu} - m}{T_f}\right), \quad (18)$$

$$V_p = 4\pi m^2 T_f K_2\left(\frac{m}{T_f}\right) \exp\left(\frac{m}{T_f}\right). \quad (19)$$

When we implement a Gaussian approximation to perform the integrals in Eq. (18) we obtained:

$$V_x \approx (2\pi R_G^2) (2\pi\tau_f^2 \Delta\eta_x^2)^{1/2}, \quad (20)$$

where R_G is the Gaussian width of the transverse coordinate distribution and $\Delta\eta_x$ is the same for the space-time rapidity distribution. In the non-relativistic limit, the volume of the local momentum-space distribution can be simplified as:

$$V_p \approx (2\pi m T_f)^{3/2}. \quad (21)$$

These leading order Gaussian limiting cases and approximations will be discussed and elaborated further in the sub-section on the discussion of the scaling properties of the longitudinal HBT-radii R_{long} , in subsection 3.3. For now, the key point of this sub-section was that in order to evaluate the mean multiplicity, we can perform the invariant integrals over the momentum variables first, going to the local rest frame at each point on the freeze-out hypersurface if on these hypersurfaces the

8 *G. Kasza, T. Csörgő*

temperature has an approximately constant value of T_f . This way a Jüttner prefactor can be pulled out with the average value of the fugacity and the remaining integral will be the average phase-space density multiplied by the total freeze-out volume (in coordinate-space) of the fireball.

3.2. Pseudorapidity density

As detailed in Refs. 16, 17 the analytic expression of the rapidity distribution was calculated by an advanced saddle-point integration to yield

$$\frac{dN}{dy} \approx \frac{dN}{dy} \Big|_{y=0} \cosh^{-\frac{1}{2}\alpha(\kappa, \lambda)-1} \left(\frac{y}{\alpha(1, \lambda)} \right) \exp \left(-\frac{m}{T_{\text{eff}}} \left[\cosh^{\alpha(\kappa, \lambda)} \left(\frac{y}{\alpha(1, \lambda)} \right) - 1 \right] \right). \quad (22)$$

The explicit expression for the normalization constant $\frac{dN}{dy} \Big|_{y=0}$ as a function of fit parameters is given by Eq. (36) of Ref. 16. From now on, we recommend to use the rapidity density at mid-rapidity as a normalization parameter fitted to data, or, as a directly measured quantity.

In this equation $y = \frac{1}{2} \ln \left(\frac{E+p_z}{E-p_z} \right)$ stands for the rapidity, the four-momentum is defined as $p^\mu = (E, p_x, p_y, p_z)$ with $E = \sqrt{m^2 + p^2}$, where the modulus of the three-momentum is $p = \sqrt{p_x^2 + p_y^2 + p_z^2}$ and m stands for the particle mass. The slope parameter of the transverse momentum spectrum is denoted as T_{eff} , standing for an effective temperature, and in order to simplify the notation we also introduce the auxiliary function α defined as

$$\alpha(\kappa, \lambda) = \frac{2\lambda - \kappa}{\lambda - \kappa}. \quad (23)$$

Note that in our earlier papers, the dependence of this function α on one of its variables, λ was suppressed, using effectively an $\alpha \equiv \alpha(\kappa, \lambda) \equiv \alpha(\kappa)$ notation in our earlier publications. From now on, we use a new, more explicit notation of $\alpha(\kappa, \lambda)$, to denote the same function but also to make the λ dependence of our results more transparent.

It is worthwhile to mention, that Eq. (22) can be further approximated in the mid-rapidity region, provided that $|y| \ll \alpha(1, \lambda) = \frac{2\lambda-1}{\lambda-1} = 2 + \frac{1}{\lambda-1}$. Obviously the domain in rapidity where such a nearly Gaussian approximation is valid, is increasing quickly as the shape parameter approaches the boost-invariant $\lambda \rightarrow 1$ limit. In such a leading order Gaussian approximation, the rapidity distribution reads as

$$\frac{dN}{dy} \approx \frac{\langle N \rangle}{(2\pi\Delta^2 y)^{1/2}} \exp \left(-\frac{y^2}{2\Delta^2 y} \right). \quad (24)$$

In this Gaussian approximation, the midrapidity density and the Gaussian width of the rapidity distribution can be expressed with the parameters of the CKCJ solution

embedded to 1+3 dimensions as follows:

$$\left. \frac{dN}{dy} \right|_{y=0} = \frac{\langle N \rangle}{(2\pi\Delta^2 y)^{\frac{1}{2}}}, \quad (25)$$

$$\frac{1}{\Delta^2 y} = (\lambda - 1)^2 \left[1 + \left(1 - \frac{1}{\kappa} \right) \left(\frac{1}{2} + \frac{m}{T_{\text{eff}}} \right) \right]. \quad (26)$$

where the mean multiplicity is given by Eq. (16), also as a function of the parameters of the embedded exact solutions is given by Eq. (36) of Ref. 16, with the replacement of $T_f \rightarrow T_{\text{eff}}$ in that equation. As mentioned before, in this paper we prefer to carry on the midrapidity density or the mean multiplicity as one of our fit parameters.

In this approximation, one may use the mean multiplicity $\langle N \rangle$ and the width of the rapidity distribution, Δy , as the relevant fit parameters, instead of the original four fit parameters of the CKCJ solution of relativistic hydrodynamics.

This result is a beautiful example of hydrodynamical scaling behaviour: although the CKCJ exact solution at the time of the freeze-out predicts that the observables will depend on four different parameters, $\left. \frac{dN}{dy} \right|_{y=0}$, κ , λ , and T_{eff} , actually in the $\lambda \rightarrow 1$ limiting case a scaling behaviour is found: the rapidity density becomes a function of only two combinations of its four physical fit parameters. So different physical fit parameters may result in the same rapidity density, if the two relevant combinations of the fit parameters remain the same.

From this shape it is also clear that the rapidity densities can be normalized both to the mid-rapidity density as well as to the total multiplicity. For an nearly boost-invariant fireball, a nearly boost-invariant distribution is obtained, and in this case its normalization to the mid-rapidity density remains valid in the boost-invariant, $\lambda \rightarrow 1$ limit too, although in this limit both the mean multiplicity and the width parameter of the rapidity density diverge.

By a saddle-point integration of the double differential spectra,^{16,17} the pseudorapidity density can also be calculated as a parametric curve, where the parameter is the rapidity y :

$$\left(\eta_p(y), \frac{dN}{d\eta_p}(y) \right) = \left(\frac{1}{2} \log \left[\frac{\bar{p}(y) + \bar{p}_z(y)}{\bar{p}(y) - \bar{p}_z(y)} \right], \frac{\bar{p}(y)}{\bar{E}(y)} \frac{dN}{dy} \right). \quad (27)$$

The pseudorapidity is denoted by $\eta_p = \frac{1}{2} \ln \left(\frac{p+p_z}{p-p_z} \right)$. The average of the momentum space variable q is indicated by \bar{q} , as given in details in Ref. 17. In order to obtain the pseudorapidity density as an analytic function of η_p , we calculated the rapidity dependent average transverse mass of the particles:

$$\bar{m}_T(y) = \int_m^\infty m_T \left(\frac{dN}{dy} \right)^{-1} \frac{dN}{dm_T dy} dm_T. \quad (28)$$

To perform the integral we used saddle-point integration method which led us to

10 *G. Kasza, T. Csörgő*

the following function:

$$\bar{m}_T(y) \simeq m + \frac{T_{\text{eff}}}{\cosh^{\alpha(\kappa, \lambda)}\left(\frac{y}{\alpha(1, \lambda)}\right)}. \quad (29)$$

From the above (29), one can obtain the rapidity dependent average energy, average longitudinal momentum and average of the modulus of the three momentum as:

$$\bar{E}(y) = \bar{m}_T(y) \cosh(y), \quad (30)$$

$$\bar{p}_z(y) = \bar{m}_T(y) \sinh(y), \quad (31)$$

$$\bar{p}(y) = \sqrt{\bar{E}(y)^2 - m^2}, \quad (32)$$

$$\bar{p}_T(y) = \sqrt{\bar{m}_T(y)^2 - m^2}. \quad (33)$$

Using these results of the saddle-point integration, the Jacobian term in Eq. (27) can be written as

$$\frac{\bar{p}(y)}{\bar{E}(y)} \equiv J(y) = \sqrt{1 - \frac{m^2}{\bar{m}_T(y)^2 \cosh^2(y)}}. \quad (34)$$

Using the above equations, the pseudorapidity can be expressed in terms of rapidity as follows:

$$\eta_p(y) = \tanh^{-1} \left(\frac{\tanh(y)}{\sqrt{1 - \frac{m^2}{\bar{m}_T(y)^2 \cosh^2(y)}}} \right), \quad (35)$$

This relation is valid for a rapidity dependent average transverse mass $\bar{m}_T(y)$ and in general it cannot be inverted. In this case, the parametric expression of the pseudorapidity distribution, given in Eq. (27) can be used for data fitting.

We have seen above that the average transverse mass $\bar{m}_T(y)$ is, to a leading order, independent of the rapidity y , if $\lambda - 1 \ll 1$. In this approximation, $\cosh^{\alpha(\kappa, \lambda)}\left(\frac{y}{\alpha(1, \lambda)}\right) \approx 1$, and the average transverse mass becomes rapidity independent, $\bar{m}_T(y) \approx \bar{m}_T(y=0)$. If $\lambda - 1 \ll 1$, we can utilize this approximation to obtain an explicit formula for the pseudorapidity density distribution from the CKCJ solution.

If $\lambda - 1 \ll 1$ and $\bar{m}_T(y) \approx \bar{m}_T(y=0)$, the following relations are also valid:

$$\bar{p}_T \approx \sqrt{(m + T_{\text{eff}})^2 - m^2} = M, \quad (36)$$

$$\bar{p}(\eta_p) \approx M \cosh(\eta_p), \quad (37)$$

$$\bar{p}_z(\eta_p) \approx M \sinh(\eta_p), \quad (38)$$

$$\bar{E}(\eta_p) \approx \sqrt{m^2 + M^2 \cosh^2(\eta_p)}. \quad (39)$$

At this point, in order to simplify the subsequent formulas, let us introduce a new variable $D = m/M$, with an important meaning to be explained later, when the

physical meaning of D becomes clear:

$$D^2 = \frac{m^2}{M^2}, \quad (40)$$

$$J(\eta_p) = \frac{\bar{p}(\eta_p)}{\bar{E}(\eta_p)} \approx \frac{\cosh(\eta_p)}{\sqrt{D^2 + \cosh^2(\eta_p)}}, \quad (41)$$

$$y(\eta_p) \approx \tanh^{-1} \left(\frac{\cosh(\eta_p)}{\sqrt{D^2 + \cosh^2(\eta_p)}} \tanh(\eta_p) \right), \quad (42)$$

where $\tanh^{-1}(z)$ is the inverse function of the tangent hyperbolic function.

Using the above equations, we find the explicit formula for the pseudorapidity distribution as follows:

$$\frac{dN}{d\eta_p} \approx \frac{\langle N \rangle}{(2\pi\Delta^2 y)^{1/2}} \frac{\cosh(\eta_p)}{(D^2 + \cosh^2(\eta_p))^{1/2}} \exp \left(-\frac{y^2}{2\Delta^2 y} \right) \Big|_{y=y(\eta_p)} \quad (43)$$

where the pseudorapidity dependence of the rapidity is given by Eq. (42).

This formula clarifies the physical meaning of the dimensionless parameter D . Actually, D^2 is a dimensionless depression parameter, or dip parameter: it controls the depth of the dip around midrapidity in the pseudorapidity distribution. At large pseudorapidities, the $dN/d\eta_p$ distribution follows the shape of the rapidity distribution, but at mid-rapidity, it is depressed, up to a factor of $1/\sqrt{1+D^2}$, as compared to the rapidity distribution. The rapidity distribution is given as a function in Eq. (22), that is obtained using a saddle-point integration technique. Although this advanced calculation suggests that the rapidity density is non-Gaussian, near mid-rapidity, this non-Gaussian function can be approximated by a Gaussian shape, as given in Eq. (24). However, to measure the rapidity distribution, particle identification is necessary, so in practice the LHC experiments typically publish first the pseudo-rapidity distribution.

We have evaluated the pseudo-rapidity distribution of the CKCJ solution, too, and our best analytic result, based on a saddle-point integration technique is given as a parametric curve in Eq. (27), derived first in Refs. 16. The applications of these formulae were detailed recently in Ref. 17. In practice, it is also possible to test, if the Gaussian approximation (to the rapidity distribution, dN/dy) is satisfactory or not, by fitting (the pseudorapidity distribution, $dN/d\eta_p$) using Eqs. (24), (25), (42) and (43). If such a fit turned out to be not satisfactory for a given dataset and a given experimental precision, one can attempt an improved fit using the more precise Eq. (22) together with Eqs. (42) and (43) to describe the experimental data on the pseudorapidity distribution. Given that the Gaussian approximation is suspected to fail at LHC energies, we recommend to start directly with this method, approximating the experimental rapidity distribution with Eq. (22).

Phenomenologically, one may fit the pseudorapidity distribution by the explicit but approximate function of Eq. (43) as well. On this crudest level of approximation,

the pseudorapidity distribution depends only on 3 parameters: the normalization $\left.\frac{dN}{dy}\right|_{y=0}$, the width parameter $\Delta^2 y$, and the dimensionless dip parameter D^2 . Similarly, one may test if the rapidity distribution can be approximated, within the experimental uncertainties, with the Gaussian form of Eq. (24). If such a Gaussian approximation describes a certain set of experimental data, the normalization constant $\left.\frac{dN}{dy}\right|_{y=0}$ can be expressed in terms of the mean multiplicity $\langle N \rangle$, as given in Eq. (25).

This result, Eq. (43) is yet another beautiful example of a hydrodynamical scaling behaviour: although the CKCJ exact solution at the time of the freeze-out predicts that the observables will depend on four different parameters, $\left.\frac{dN}{dy}\right|_{y=0}$, κ , λ and T_{eff} , actually in the $\lambda \rightarrow 1$ limiting case a scaling behaviour is found and the pseudo-rapidity density becomes a function of only three combinations of the four physical fit parameters, namely $\langle N \rangle$, Δy and D .

We expect that these nearly Gaussian approximations are valid only in a certain limited range of rapidities or pseudo-rapidities, typically up to 2, 2.5 units away from mid-rapidity, as detailed in Refs. 16, 17. We also expect that the range of validity of the more precise Eq. (22) is a broader interval in y or in η , as compared to the simplified Gaussian form of Eq. (24). References 16, 17 detail the *maximum* of the (pseudo)rapidity range, where the fits with Eqs. (22) and (27) are expected to work. These limits of the domain of the validity of these fits are expressed there in terms of the fit parameters. One of the open questions seems to be that apparently the fits seem to work better and in a larger pseudo-rapidity range, as they are expected, as demonstrated on Xe+Xe data at LHC energies in section 4.

We may conjecture, that the derivation of these analytic formulae to fit the (pseudo)rapidity densities can possibly be generalized and extended to a broader class of exact solutions of relativistic hydrodynamics and to a larger range of (pseudo)rapidities. To check this conjecture, it is necessary to search for suitable generalizations or extensions of the CKCJ family of solutions.¹⁶ However, the detailed investigation of such possible generalizations of an already published exact solution goes also well beyond the limitations of our current manuscript.

In short, the pseudorapidity distribution of Eq. (43) is fully specified and given as a function of η_p , and the fit range is also well defined and limited to a finite interval around mid-rapidity. This Eq. (43) is now given as an explicit function of the pseudo-rapidity. Let us emphasize, that this function is obtained from the parametric curve of Eq. (27) in the $\lambda - 1 \ll 1$ approximation, that results in the $\cosh^{\alpha(\kappa, \lambda)}\left(\frac{y}{\alpha(1, \lambda)}\right) \approx 1 + \mathcal{O}((\lambda - 1)^2)$ approximation. This approximation is very useful, but its validity has to be checked when a given data-set is analyzed - in principle, the parametric curve of Eq. (27) it also implies that the average transverse momentum \bar{p}_T is approximately independent of the longitudinal momentum component, if Eq. (43) is a valid approximation. These formulae are well suited for data fitting, as shown for example on Fig. 3.

To describe measurements by fits of formulae, let us clarify that Eq. (27) depends on four fit parameters that are listed as follows:

- (1) the average speed of sound $c_s = 1/\sqrt{\kappa}$, that corresponds to the equation of state,
- (2) the effective temperature T_{eff} that corresponds to the slope of the $m_T - m$ spectra at mid-rapidity,
- (3) the parameter λ , that controls the relativistic acceleration of the fluid,
- (4) and $dN/dy|_{y=0}$, the normalization at midrapidity, that corresponds to the particle density at midrapidity.

When comparing to measured $dN/d\eta_p$ data, we take κ from the measurement of the PHENIX Collaboration, Ref. 24, T_{eff} is also taken from the experimentally determined transverse momentum spectra, so from fits to the rapidity or pseudorapidity distributions of Ref. 26, one obtains the shape and the normalization parameters λ and $dN/dy|_{y=0}$, respectively. See Refs. 16, 17 for further details and applications.

In the Gaussian approximation, the speed of sound or equation of state and the effective temperature T_{eff} enter to the fit only through their combination that determines the width parameter $\Delta^2 y$, so instead of two independent fit parameters of T_{eff} and κ only their combination $\Delta^2 y$ can be determined from the data. Assuming a given value of κ , the effective temperature T_{eff} can be determined from the width parameter $\Delta^2 y$ using Eq. (26). In this Gaussian approximation, the pseudo-rapidity density can thus be described by three parameters, itemized as follows:

- (1) the mean multiplicity $\langle N \rangle$ that controls the normalization,
- (2) the width parameter Δy that controls the width,
- (3) and dip parameter D , that controls the depth of the $dN/d\eta_p$ distribution at mid-rapidity.

As a closing remark for this subsection, let us emphasize that in the midrapidity region (where $y \approx 0$) one can go beyond the rapidity independent mean p_T approximation of Eq. (36) by evaluating the leading, second order correction terms as a function of y . The resulting rapidity dependent average transverse mass is obtained to have a Lorentz distribution as follows:

$$T_{\text{eff}}(y) \equiv \bar{m}_T(y) - m = \frac{T_{\text{eff}}}{1 + a y^2}, \quad (44)$$

where the physical meaning of the effective temperature T_{eff} becomes clear as the mean (thermally averaged) transverse mass at mid-rapidity. The parameter a that controls the width of this Lorentz distribution is found to depend on a combination of the equation of state parameter κ and on the acceleration parameter λ as

$$a = \frac{1}{2} \frac{\alpha(\kappa, \lambda)}{\alpha^2(1, \lambda)}. \quad (45)$$

Note, that such a Lorentzian rapidity dependence for the slope of the transverse momentum spectra has been derived from analytic hydrodynamics first in Ref. 27, assuming a scaling Bjorken flow in the longitudinal direction but with a Gaussian

density profile. As far as we know, the EHS/NA22 collaboration has been the first to perform a detailed and combined hydrodynamical analysis of single-particle spectra and two-particle Bose–Einstein correlations in high energy physics in Ref. 4. Although the derivation is valid only for symmetric collisions, a Lorentzian shape of the rapidity dependent average transverse momentum has been observed, within errors, by the EHS/NA22 experiment in Ref. 4 in the slightly asymmetric hadron-proton collisions, using a mixed π^+/K^+ beam with a laboratory momentum of 250 GeV/c.

The above result, Eq. (44) is our third beautiful example of hydrodynamical scaling behaviours: although the CKCJ exact solution at the time of the freeze-out predicts that the observables will depend on four different parameters, $\left.\frac{dN}{dy}\right|_{y=0}$, κ , λ and T_{eff} , actually in the $\lambda \rightarrow 1$ limiting case a data collapsing behaviour is found and the rapidity dependent mean transverse momentum becomes a function of only on T_{eff} and on combination of the two different physical fit parameters κ and λ , denoted as a and defined in Eq. (45).

3.3. Longitudinal HBT-radii

As discussed in Ref. 27, for a 1+1 dimensional relativistic source, in a Gaussian approximation the relative momentum dependent part of the two-particle Bose–Einstein correlation function is characterized by (generally mean pair momentum dependent) longitudinal Hanbury-Brown Twiss (HBT) radii. The general expression in the longitudinally co-moving system (LCMS), where the mean momentum of the pair has zero longitudinal component, reads²⁷ as

$$R_{\text{long}}^2 = \cosh^2(\eta_x^s) \tau_f^2 \Delta\eta_x^2 + \sinh^2(\eta_x^s) \Delta\tau^2. \quad (46)$$

Here (τ_f, η_x^s) stands for the Rindler coordinates of the main emission point of the source in the (t, r_z) plane, which are derived from a saddle-point calculation of the rapidity density, and including τ_f , the lifetime parameter of the fireball. The $\Delta\tau$ and $\Delta\eta_x$ characteristic sizes define the main emission region around the saddle-point at (τ_f, η_x^s) . For R_{long} measurements at midrapidity, where $\eta_x^s \approx 0$, this formula can be simplified as

$$R_{\text{long}} = \tau_f \Delta\eta_x. \quad (47)$$

If the emission function of particles with $y=0$ can be well approximated by a Gaussian shape, with $\Delta\eta_x$ being the width of the space-time rapidity distribution of these particles with vanishing momentum-space rapidity, the longitudinal HBT-radii at $y=0$ can be derived from the CKCJ solutions as we have already shown in Ref. 19:

$$R_{\text{long}} = \tau_f \Delta\eta_x \approx \frac{\tau_f}{\sqrt{\lambda(2\lambda-1)}} \sqrt{\frac{T_f}{m_T}}, \quad (48)$$

where the transverse mass of the particles is denoted by $m_T = \sqrt{m^2 + p_T^2}$, and T_f stands for the freeze-out temperature that can be extracted from the analysis of

the transverse momentum spectra. Note that in general $T_f < T_{\text{eff}}$ as the effective temperature of the transverse momentum spectra contains not only the freeze-out temperature but also radial flow and vorticity effects, see Refs. 22, 28, 29.

Importantly, Eq. (48) is found to depend on the acceleration parameter λ that characterizes the CKCJ solutions, and to be independent of the κ parameter, that characterizes the speed of sound and the Equation of State. It is interesting to note that this result corrects the $R_{\text{long}} \approx \frac{\tau_f}{\lambda} \sqrt{\frac{T_f}{m_T}}$ approximation of Csörgő, Nagy and Csanád (CNC) in Refs. 30, 31, obtained in the $\kappa \rightarrow 1$ limit. The effect of the accelerating trajectories is corrected by Eq. (48) by a $\lambda \rightarrow \sqrt{\lambda(2\lambda - 1)}$ transformation in the CNC estimate for R_{long} , Refs. 30, 31. In the boost invariant limit ($\lambda \rightarrow 1$), the longitudinal radii of the CKCJ solution and the CNC solution both reproduce the same Makhlin - Sinyukov formula of Ref. 32.

3.4. Scaling properties of R_{long} with (pseudo)rapidity density

Recently, the ALICE collaboration reported,³³ that the cubed HBT radii scale with the pseudorapidity density in a broad energy region including SPS, RHIC and LHC energies and in a broad geometry region including $p+p$, $p+A$ and $A+A$ collisions. Similar scaling laws have been observed by the PHENIX and STAR Collaborations, that suggested that each of the main the HBT radii ($i = \text{side, out and long}$) follow the $R_i \propto N_{\text{part}}^{1/3}$ scaling in $\sqrt{s_{NN}} = 200$ GeV Au+Au collisions.^{34, 35} Earlier, the CERES collaboration reported that the HBT volume $R_{\text{side}}^2 R_{\text{long}}$ is proportional to N_{part} , the number of participants.³⁶ Ref. 37 observed that the N_{part} scaling of the HBT radii can likely be due to the linear correlation between N_{part} and the $dN/d\eta_p$ at mid-rapidity. Recently such a proportionality of the HBT radii and the pseudo-rapidity density was demonstrated on a broad class of data from high multiplicity pp through pA and AA collisions by the ALICE collaboration in Ref. 33. However, as far as we know, the $R_{\text{HBT}} \propto \left(\frac{dN}{d\eta_p}\right)^{1/3}$ scaling law has not been derived so far from any exact solution of (relativistic) fireball hydrodynamics.

It is thus a valid question if our solution can reproduce the energy-independent scaling that corresponds to Fig. 9 of Ref. 33 in a straight-forward manner, or not. Let us investigate this question briefly as follows:

From Eq. (17) one finds that the average multiplicity $\langle N \rangle$ depends on the system size V_x and on the freeze-out temperature T_f through the phase space volume. According to Eq. (48), the freeze-out temperature can be expressed by the longitudinal radius R_{long} . As the freeze-out temperature T_f is an m_T independent constant and it can be expressed as a product of two, transverse mass dependent factors, we can evaluate this relation also at the average transverse mass \bar{m}_T to find

$$T_f = \frac{m_T \lambda (2\lambda - 1)}{\tau_f^2} R_{\text{long}}^2 = \frac{\bar{m}_T \lambda (2\lambda - 1)}{\tau_f^2} \bar{R}_{\text{long}}^2. \quad (49)$$

Therefore from Eqs. (17) and (21) it is easy to see that the mean multiplicity

16 *G. Kasza, T. Csörgő*

$\langle N \rangle$ depends on the (m_T averaged) longitudinal radius, \bar{R}_{long} as:

$$\langle N \rangle \propto V_x T_f^{3/2} \propto V_x \bar{R}_{\text{long}}^3. \quad (50)$$

Note, that the mean multiplicity $\langle N \rangle$ also depends on the system size, as it is proportional to the total geometrical volume of the fireball at the mean freeze-out time. Note also that the constant of proportionality $T_f^{3/2}$ depends on the *local* freeze-out temperature T_f , as it is the measure of the size of the momentum space in the local comoving system.

The proportionality of the pseudorapidity density and R_{long}^3 , as discussed in Ref. 33, is straightforward to derive from the CKCJ solution. This proportionality directly follows from the proportionality of Eq. (50) and the relation

$$\frac{dN}{d\eta_p} = \langle N \rangle \rho(\eta_p), \quad (51)$$

where $\rho(\eta_p)$ is the normalized pseudorapidity density, with the following normalization condition:

$$\int_{-\infty}^{\infty} \rho(\eta_p) d\eta_p = 1. \quad (52)$$

Thus the pseudorapidity distribution is proportional to the mean multiplicity (times a probability density). As the mean multiplicity depends on the (transverse mass averaged) longitudinal HBT-radii as well as on the average transverse mass, we find that

$$\left. \frac{dN}{d\eta_p} \right|_{\eta_p=0} = \langle N \rangle \rho(\eta_p=0) \propto \bar{R}_{\text{long}}^3. \quad (53)$$

In other words, at mid-rapidity, $\eta_p \approx 0$,

$$\bar{R}_{\text{long}} = A \left(\frac{dN}{d\eta_p} \right)^{\frac{1}{3}}, \quad (54)$$

where the constant of proportionality A is actually a complicated function of quantities that may depend on the expansion dynamics in a non-trivial manner. It is clear that A depends on V_x/τ_f^3 , on the acceleration parameter λ , on the width of the rapidity distribution Δy hence on the (temperature averaged) speed of sound $c_s^2 = 1/\kappa$, on the effective temperature T_{eff} , on the mass of the particles m and on the average phase-space occupancy \bar{f} . A good strategy can be to take the value of A directly from measurements. Experimentally, A is found to be weakly dependent on the system size, increasing for larger systems. We need to do more detailed data fitting to cross-check the properties of A , than doable within the limits of the current investigations.

For the present paper, let us emphasize only that the proportionality of Eq. (54) is a natural consequence of the investigated CKCJ solution of Ref. 16. This is due to the fact that the local freeze-out temperature determines the size of homogeneities at the time of freeze-out, when the geometrical sizes of the expanding system is

large (Refs. 27, 32), $R_{HBT} \propto T_f^{1/2}$. The same local freeze-out temperature on the power of $3/2$, $T_f^{3/2}$ measures the local volume of the momentum space which multiplied together with the total volume of the fireball is proportional to the mean multiplicity, hence the pseudorapidity density. Thus the transverse mass averaged HBT radii scale as $\bar{R}_{HBT} = A \left(\frac{dN}{d\eta_p} \right)^{\frac{1}{3}}$, for expansion dominated systems with larger geometrical than thermal length-scales, as noted in Ref. 27. This scaling is expected to break down at low energies where the expansion effects are less important and the geometrical sizes start to dominate the HBT radii.

The above result is formulated in a general manner, and it is valid in a broad class of 1+1 and 1+3 dimensional exact solutions of (relativistic) hydrodynamics. For example, it is valid for several classes of 1+1 dimensional relativistic hydrodynamical solutions, including the CKCJ solution of Refs. 16,17 and the CNC solution of Refs. 30,31. Although the Bjorken-Hwa solution of Refs. 3,38 leads to a flat rapidity density distribution, it can be considered as the $\lambda \rightarrow 1$ limiting case of our description. Hence the scaling law of the longitudinal HBT radius as expressed by Eq. (54) is proven here to be valid for the boost-invariant Hwa-Bjorken solution, too.

We also find, that the validity of this derivation can be extended to the non-relativistic kinematic domain, where $m_T \approx m$, and the same result is obtained for the 1+3 dimensional, non-relativistic exact solutions of fireball hydrodynamics of Refs. 20,22,39–41, extending the derivation not only to the longitudinal HBT radius but also to the transverse (side, and out) HBT radii.

Our derivation provides a novel method that can be applied in a broader and more general class of exact solutions of fireball hydrodynamics than the considered 1+1 dimensional CKCJ solution. It seems to us that the key steps are the proportionality of the mid-rapidity pseudorapidity density to the average HBT volume (evaluated at mid-rapidity and at the average value of the transverse momentum) times the volume of the invariant momentum distribution (in momentum-space). Another way to consider this result is to note that when evaluating the mean multiplicity, the order of the invariant integration over the momentum distribution and the integration over the freeze-out hypersurface is exchangeable.

A detailed exploration of this topic and the generalization of our method to other exact solutions of relativistic hydrodynamics looks indeed very promising and attractive. A more detailed proof of these deep properties of exact solutions of fireball hydrodynamics goes, however, well beyond the scope of our present manuscript, that focusses on the exploration of the experimental consequences and observable relations that can be derived from the CKCJ family of exact solutions of relativistic fireball hydrodynamics in 1+1 dimensions.

4. Data analysis and fit results

In what follows, let us detail and explain, how one can improve on Bjorken's estimate for the initial energy density, using straightforward fits to the already published data and relying on exact results from 1+1 dimensional relativistic hydrodynamics.

To extract τ_f , the lifetime parameter of the fireball, we fit the pseudorapidity density to extract the shape parameter λ , and the longitudinal HBT-radius of the CKCJ solution to the experimental data. For comparisons of the consequences of the CKCJ hydro solutions with measurements, we have selected data on $\sqrt{s_{NN}} = 130$ GeV and 200 GeV Au+Au collisions, because the pseudorapidity density, the slope parameter of the transverse momentum spectra and the HBT radii are known to be measured in the same, 0-30% centrality class. In both of these reactions, the PHENIX collaboration published their two-pion correlation results in the 0-30% centrality class, consequently we fitted our hydrodynamic model to the pseudorapidity density data of PHOBOS experiment from Ref. 26, that we averaged in this 0-30 % centrality class. The centrality dependence of the effective temperature can be estimated with the help of an empirical relation,

$$T_{\text{eff}} = T_f + m \langle u_T \rangle^2. \quad (55)$$

This relation has been derived for a three-dimensionally expanding, ellipsoidally symmetric exact solution of fireball hydrodynamics with a temperature dependent speed of sound, as a model for non-central heavy ion collisions,²⁰ but only for a single kind of hadron that had a fixed mass m . Recently this relation has also been re-derived for a non-relativistic, 3 dimensionally expanding fireball that hadronizes to a mixture of various hadrons that have different masses m_i just like a mixture of pions, kaons and protons, as detailed in Ref. 42. This derivation included a lattice QCD EoS in the quark matter or strongly interacting quark gluon plasma phase.⁴²

It is remarkable that the rotation or vorticity of the nearly perfect fluid of Quark-Gluon Plasma⁹ does not change the affine-linear relation between the effective temperature and the mass of particles. As it was shown in Ref. 41 the transverse flow $\langle u_T \rangle$ in Eq. (55) can be identified with a quadratic sum of the radial flow \dot{R}_f and the tangential flow that corresponds to the rotation of the fluid, $\omega_f R_f$ as

$$\langle u_T \rangle^2 = \dot{R}_f^2 + \omega_f^2 R_f^2, \quad (56)$$

where at the time of the freeze-out, R_f is the transverse radius of an expanding and rotating fireball, \dot{R}_f stands for the radial flow ie the time derivative of $R(t)$ at the freeze-out time t_f and ω_f is the angular velocity of the rotating fireball at the freeze-out time t_f . This relation was derived, as far as we know, for the first time in Ref. 41, using a lattice QCD motivated equation of state, for a general temperature dependent speed of sound given by $\kappa(T)$, assuming a spheroidal symmetry and non-relativistic kinematics. This derivation was generalized to a triaxial, rotating and expanding fireball in Ref. 28, that found that $R_f = 0.5(X_f + Z_f)$ is the average freeze-out radius for a fireball rotating around the transverse (r_y) axis and off-diagonal terms correspond to the difference of the rotating and expanding motion

of the fluid within the triaxial ellipsoid and the rotating and expanding motion of geometrical shape of the triaxial ellipsoid.²⁸

Due to both radial flow and vorticity effects, $\langle u_T \rangle$, the slope of the affine-linear function in Eq. (55) is expected (and experimentally found) to be significantly centrality dependent. On the other hand, the intercept of this affine-linear function, T_f is interpreted as the freeze-out temperature, that is expected (and experimentally found) to be centrality independent. The numerical value of T_f is empirically found from the analysis of the transverse momentum spectrum and it is indeed approximately independent of the particle type, the centrality and the center of mass energy of the collision. Figure 1 illustrates the linear fits to the effective temperature of charged pions, charged kaons, and protons, antiprotons for PHENIX Au+Au at $\sqrt{s_{NN}}=130$ GeV and 200 GeV data, and suggests that the T_f value that is consistent with this interpretation of the transverse momentum spectra is $T_f \approx 175$ MeV for both $\sqrt{s_{NN}} = 130$ and 200 GeV Au+Au collisions, independently of particle mass, centrality and center of mass energy of the collision indeed. Important theoretical expectations suggests a lower value for the freeze-out temperature, corresponding to the mass of the lightest strongly interacting quanta with no conserved charge, $T_f \approx m_\pi$, the pion mass. Thus we have also investigated if $T_f = 140$ MeV can be utilized for the extraction of the life-time of the reaction. Lower freeze-out temperatures correspond to larger life-times for the same datasets according to Eq. (48), and we shall subsequently see that longer life-times correspond to larger initial energy densities for the same pseudorapidity distributions. In what follows, we utilize the more conservative, shorter life-times obtained with larger freeze-out temperatures in Table 1. These values give lower estimates for the initial energy densities. However, we also test the effects the possible longer lifetimes and larger initial energy densities, corresponding to the lower value of $T_f = 140$ MeV. We summarize the corresponding longer freeze-out times also in Table 1, so that the interested reader may evaluate the corrections that originate from the choice of a lower freeze-out temperature to the initial energy density estimates in a straightforward manner.

If the effective temperature is allowed to be a free fit parameter in the $dN/d\eta_p$ fits, we find, that the fit results are in agreement with the estimated centrality dependence of T_{eff} that are determined from Fig. (1). As the pseudorapidity distributions depend not only on the effective temperature T_{eff} but also on the average speed of sound, we fixed the speed of sound to $c_s^2 = 0.1$ in accordance with the experimental results of the PHENIX collaboration.²⁴ Since the CKCJ solution is valid in a limited, central pseudorapidity interval only, we fitted the $\frac{dN}{d\eta_p}$ of the CKCJ solution to data in the $[-2.5, 2.5]$ pseudorapidity interval. The fits and the best fit parameters are shown on Figure 2.

It is important for the current study, that T_{eff} , $\frac{dN}{d\eta_p}$ and R_{long} must be determined in the same centrality class of the same colliding system at the same energy. As it can be seen on the right panel of Fig. 1, for Au+Au at $\sqrt{s_{NN}}=200$ GeV, T_{eff} data are available in the 0-5 % and 40-50 % centrality classes, but they were not directly measured in the 0-30 % centrality class. Note that the $T_{\text{eff}} = 203$ MeV value

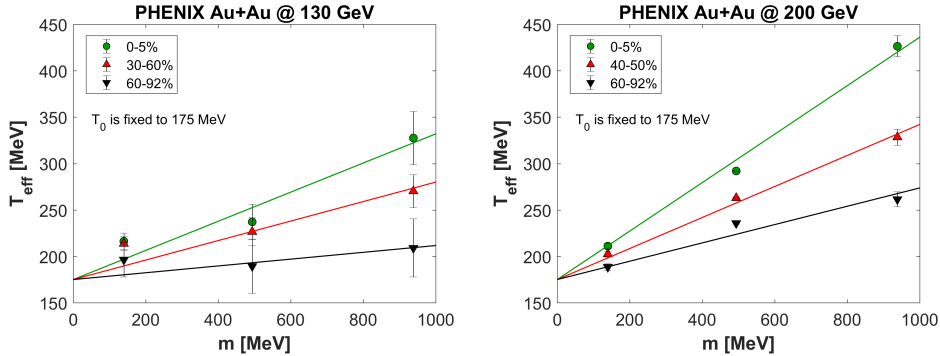
20 *G. Kasza, T. Csörgő*

Figure 1. The mass and centrality dependence of the effective temperature of charged pions and kaons, as well as protons and anti-protons in $\sqrt{s_{NN}} = 130$ GeV (Ref. 43) and $\sqrt{s_{NN}} = 200$ GeV (Ref. 44) Au+Au collisions. For each centrality classes, the linear fits are shown by continuous lines. The freeze-out temperature parameter T_f is fixed to 175 MeV in both cases, although at 130 GeV, a slightly higher $T_f \approx 180$ MeV is preferred by the data.

that we obtained from fitting the $\frac{dN}{d\eta_p}$ data at $\sqrt{s_{NN}} = 200$ GeV for the 0-30 % centrality class is just in between the values that are obtained for the 0-5 % and 40-50 % centrality classes, as indicated on Fig. 1. However, for the same system at $\sqrt{s_{NN}} = 130$ GeV, T_{eff} data are measured also in the 5-15 % and the 15-30 % centrality classes – although these are not shown on the left panel of Fig. 1. We evaluated the inverse slope for the 0-30 % centrality class by averaging the fit of the $T_{\text{eff}} = T_f + m\langle u_T \rangle^2$ relation over the 0-5 %, 5-15 % and 15-30 % centrality classes for the pion mass, and obtained values that are consistent with both the corresponding values from the $m_T - m$ spectrum fits, as indicated on Fig. 1, and from the fits of the pseudo-rapidity distributions as discussed in the next sub-section.

4.1. Fits to the pseudorapidity distribution

We describe below two kind of pseudo-rapidity distributions: first, we detail fits to Au+Au collision data at the RHIC energies at $\sqrt{s_{NN}} = 130$ and 200 GeV, then we discuss fits to recent CMS data on Xe+Xe collisions at $\sqrt{s_{NN}} = 5.44$ TeV at LHC.

4.1.1. Fits to PHOBOS data in Au+Au collisions at RHIC

The PHOBOS collaboration published an extensive study of pseudorapidity distributions in Au+Au collisions at various energies at RHIC.²⁶ Unfortunately, the point-to-point fluctuating statistical and systematic errors of the $\frac{dN}{d\eta_p}$ data are not separated from the point-to-point correlated normalization error in these publications.²⁶ This makes a simple χ^2 test practically useless, as it leads to overly small estimations for the value of χ^2 . We have analyzed these data with an advanced χ^2 test, described as follows.

As a preparatory and necessary control point, we have fitted the PHOBOS pseudorapidity distributions with our formulae of Eq. (27), using the uncertainty band, given by the PHOBOS experiment in Ref. 26 as a preliminary error estimate. Unfortunately this uncertainty band did not separate the point to point fluctuating errors from the point-to-point correlated systematic and overall correlated systematic errors. The fits were excellent from the point of view of the χ^2/NDF however they were not sufficiently well constrained to follow the shape of the data points, as the overall errors were apparently so large that the shape was not constrained too much. Because of these circumstances, we tried to estimate the point-to-point fluctuating errors and a more stringent and advanced estimated for value of χ^2 . Consequently, we have fitted the $\frac{dN}{d\eta_p}$ data in three steps, as follows:

In the first step, tried to create a smooth line that interpolates between the datapoints. In order to achieve this, we used an estimated (ad hoc) η_p independent, 3 % fluctuating uncorrelated uncertainty on each datapoint and we used these errors to minimize the value of χ^2 . Using the fitted parameters, obtained from this first step, we got a good-looking overall description that we considered as a smooth interpolating line that smoothly connects the data points, in a reasonable looking manner.

In a second step, we estimated the sum of the point-to-point fluctuating error of each data points of the $\frac{dN}{d\eta_p}$ spectra by determining the deviations of the data points from the interpolating line determined in the previous, first step, and we considered these deviations as our best estimations e_i for the fluctuating errors of data points d_i .

In the third step, we have repeated the χ^2 minimization with the data points d_i and our estimated point-to-point fluctuating errors e_i . This is the value of χ^2 and the corresponding confidence level CL that we report on Figure 2. Thus the χ^2 values, for the advanced calculations, indicated on Figure 2 are defined as:

$$\chi^2 = \sum_i \frac{\left(d_i - f(\eta_{p,i} | \kappa, \lambda, T_{\text{eff}}, \frac{dN}{dy}(y=0)) \right)^2}{e_i^2}, \quad (57)$$

where $f(\eta_{p,i} | \kappa, \lambda, T_{\text{eff}}, \frac{dN}{dy}(y=0))$ is the theoretical result given as a parametric curve, corresponding to Eqs. (22), (27) and (29)-(42) with $\kappa = 10$ fixed values and using mid-rapidity density as a normalization. Given that the values of e_i defined above correspond to the actual point-to-point fluctuations of the PHOBOS data points, that are significantly smaller as compared to the total and point-to-point correlated errors reported by PHOBOS, so our fits are required to follow the data points rather closely. A quality description of the data points can be obtained this way, as indicated on Figure 2.

As discussed in the previous section, in a Gaussian approximation only a combination of the effective temperature T_{eff} and the equation of state parameter κ enters the fitting function denoted as f_G , and another combination of the mass m and the effective temperature, D enters the fitting function. Hence the χ_G^2 distribution, that

22 *G. Kasza, T. Csörgő*

corresponds to the Gaussian rapidity distributions, is defined as follows:

$$\chi_G^2 = \sum_i \frac{\left(d_i - f_G(\eta_{p,i} | \langle N \rangle, \Delta y, D)\right)^2}{e_i^2}, \quad (58)$$

where $f_G(\eta_{p,i} | \langle N \rangle, \Delta y, D)$ is the theoretical curve in a Gaussian rapidity density approximation, corresponding to Eqs. (43), (24) and (25).

The new results indicated on Figure 2 continue the trend that was demonstrated already in Refs. 16, 17: the lower the collision energy, the greater the acceleration parameter λ , and the greater the difference from the asymptotic, boost-invariant $\lambda = 1$ limit. Note that relativistic acceleration vanishes in the boost-invariant limit, which corresponds to $\lambda = 1$.

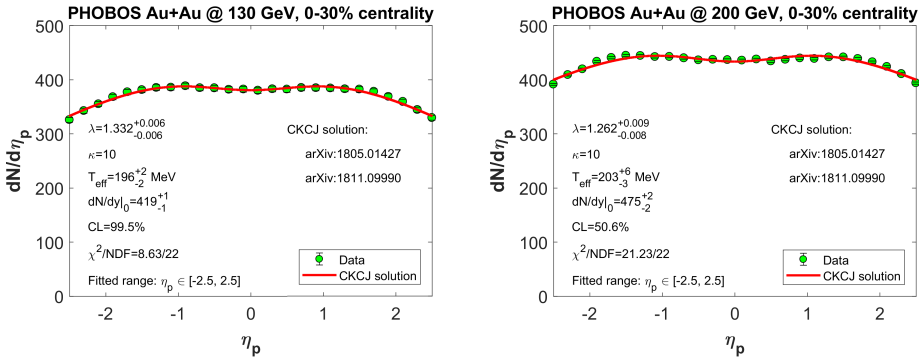


Figure 2. Fits of the pseudorapidity density with the CKCJ hydro solution,¹⁶ to PHOBOS Au+Au data at $\sqrt{s_{NN}} = 130$ GeV (Ref. 26) (left) and $\sqrt{s_{NN}} = 200$ GeV (Ref. 26) (right) in the 0-30 % centrality class. The fit quality is determined by χ^2 defined by Eq. (57) and, as usual, the number of degrees of freedom is denoted by the acronym *NDF*. The speed of sound is $c_s^2 = 1/\kappa = 0.1$, fixed in both cases. The large systematic errors on PHOBOS data are suppressed on this plot.

Since we have obtained the effective temperature T_{eff} and the acceleration parameter λ from the transverse momentum spectra and the pseudorapidity density data, the number of fit parameters in Eq. (48), i.e. in our new formula for the longitudinal HBT radii is reduced to one: the remaining free parameter is the lifetime parameter τ_f .

4.1.2. Fits to CMS data on Xe+Xe collisions

In Ref. 53, CMS collaboration published the pseudorapidity density of Xe+Xe collisions measured at $\sqrt{s_{NN}} = 5.44$ TeV in the 0-80 % centrality class. In addition, CMS compared these data to various model calculations, that were to a smaller or greater extent also influenced by numerical solutions of relativistic hydrodynamics. In particular, the comparisons included the prediction of EPOS LHC of Refs. 54, 55,

that includes a proper hydro treatment for heavy ion collisions. In case of $p+p$ collisions at LHC energies, a realistic treatment of the hydrodynamical evolution with proper hadronization such an effect was not observed in EPOS, hence the EPOS LHC model includes a non-hydrodynamically generated radial flow in small systems, like $p+p$ collisions. The HYDJET Monte Carlo simulation of Ref. 56 relies on a superposition of a soft hydro-type state and hard multi-jets. The AMPT model includes the Heavy Ion Jet Interaction Generator (HIJING) for generating the initial conditions, Zhang's Parton Cascade (ZPC) for modeling partonic scatterings, the Lund string fragmentation model or a quark coalescence model for hadronization, and A Relativistic Transport (ART) model for treating hadronic rescatterings, in an improved and combined way to give a coherent description of the dynamics of relativistic heavy ion collision.⁵⁷ Apparently, each of these models had difficulties in predicting the CMS Xe+Xe data at their present phase of development.

CMS data from Ref. 53 provided strikingly significant deviations each of these models, although each of them included a detailed simulation of resonance decays as well, while we use the core-halo model of Ref. 49 to handle phenomenologically the effect of long-lived resonances. A key property of the core-halo model of Ref. 49 is that provides an understanding and an explanation of why the hydrodynamical scaling properties can be observed in high energy heavy ion and hadron-hadron interactions even if the hydrodynamically evolving core of the reaction is surrounded by a halo of (long-lived) resonance decays. Actually the EPOS LHC calculations of Refs. 54, 55 also separate the hydrodynamically evolving core from the halo of resonance decays in a more detailed, but qualitatively similar manner to the core-halo model, but they use the core-corona terminology^{54, 55} instead of the core-halo terminology of,⁴⁹ to describe apparently similar physics ideas.

As indicated on Figs. 1 and 2 of Ref. 53, each of the AMPT 1.26t5, EPOS LHC v3400, and HYDJET 1.9 models fails to describe the pseudorapidity distribution of Xe+Xe collisions at $\sqrt{s} = 5.44$ TeV already on a qualitative level. However, we were able to describe these CMS data even with the crudest, nearly Gaussian approximation of the CKCJ solution¹⁶ of relativistic hydrodynamics, not only on a qualitative but also on a quantitative level, as indicated on Fig. 3. In fact, the CKCJ solution¹⁶ describes this recent CMS dataset surprisingly well, as detailed below.

The fit quality is statistically not unacceptable, actually our three-parameter formula of Eq. (27) provides a fine description of these CMS data. We have tested that fitting with the more precise parametric curve of Eq. (27), or using the Gaussian approximation of Eqs. (42) and (43), we obtain similarly good fit quality. From the fit parameters of the parameteric curve of Eq. (27), using the results of Refs. 16, 17, we have expected that the parameteric curve fit is able to describe these Xe Xe data in a rather limited pseudo-rapidity range, corresponding approximately to $-2.2 < \eta_p < 2.2$. In fact, Fig. 3 indicates that even in the Gaussian approximation, our fit actually describes the data significantly better, than expected.

In particular, as indicated by Fig. 3, the fit quality is satisfactory for the range of the data description, corresponding to $-3.2 < \eta_p < 3.2$, without compromising

the fit quality. This range is significantly extended, as compared to the expected $-2.2 < \eta_p < 2.2$ fit range. This is particularly interesting as we have used a hydrodynamical scaling description, where only three combinations ($\langle N \rangle$, Δy , D) of the four hydrodynamical fit parameters T_{eff} , λ , κ , and $dN/dy|_{y=0}$ are used in the data description. This is in contrast with the difficulties of the microscopic simulations mentioned above. The simplicity and powerfullness of our description reminds us the simplicity of the use of the ideal gas law, $pV = kNT$, to describe the expansion and related pressure, volume and temperature changes of an ideal gas, keeping the essential physical variables, instead of modelling such an expansion by Monte-Carlo simulations of the same process. If indeed relativistic hydrodynamics is relevant to describe the scaling properties of high energy proton-proton and heavy ion collisions, similar simplifications and data collapsing behaviour can be expected. In this paper, we have given three specific examples for scaling laws of hydrodynamical origin: the rapidity density of Eq. (24), the rapidity dependence of the effective temperature in Eq. (29) and the pseudorapidity density of Eq. (43). Each suggests such data collapsing behaviour. These new scaling laws are now rigorously derived – under certain conditions – from the CKCJ exact solutions^{16,17} of relativistic hydrodynamics. It is time to start their more detailed experimental scrutiny in various symmetric collisions of high energy particle and nuclear physics.

Fig. 3 indicates, that our fit describes the data in a larger pseudo-rapidity domain than derived in Refs. 16, 17, thus one may conjecture that perhaps the result of the derivation is more general, than the derivation itself. The search for possible generalizations of our derivation of the hydrodynamical scaling laws of the dN/dy and $dN/d\eta_p$ distributions is one of our currently open research questions.

As a possible experimental test of the relevance of the CKCJ solutions in describing high energy heavy ion collisions, we have evaluated the CKCJ prediction for the not yet measured rapidity density for Xe+Xe data at $\sqrt{s_{NN}} = 5.44$ TeV, in the 0-80 % centrality class, using the same set of parameters, that we have obtained from the pseudorapidity distributions. We have indicated our prediction for dN/dy on the same Fig. 3, as the pseudorapidity density, in order to highlight the similarities and the differences between these two, kinematically different but physically similar distributions.

4.2. Lifetime estimates for Au+Au collisions at RHIC

In order to extract the lifetime information of the fireball from Eq. (48), we compared the life-time dependent longitudinal HBT radius parameters to experimental data. Our fits to the measured values of the longitudinal HBT radii R_{long} are illustrated on Figure 4. The results are summarized in Table 1, where the systematic variation of the freeze-out time or life-time parameter τ_f with the variation of the assumed value of the freeze-out temperature T_f is also indicated. Given that longer life-times yield larger initial energy density estimates for the same pseudorapidity distribution, we evaluated the initial energy densities for the more conservative val-

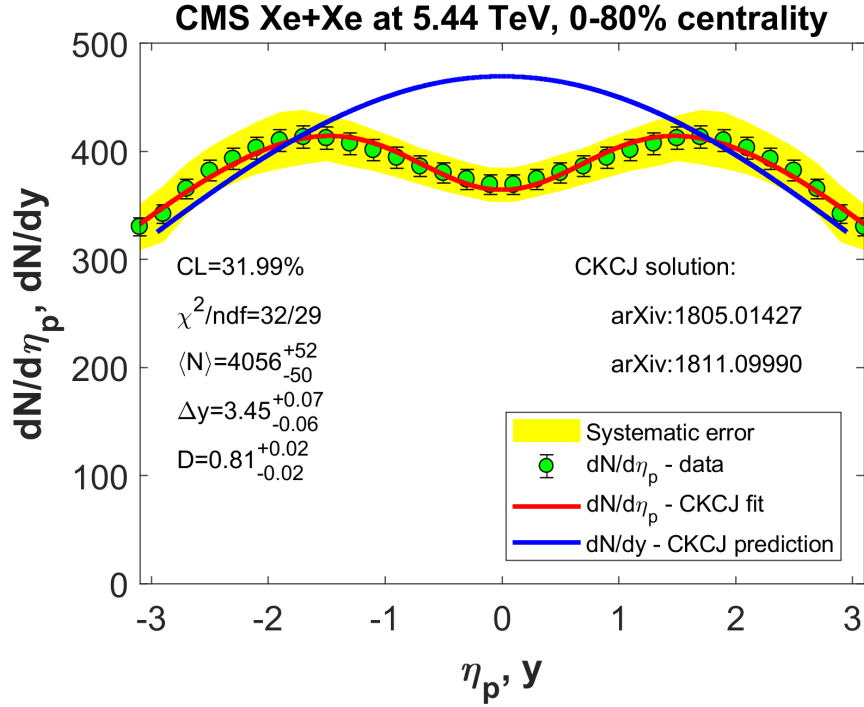


Figure 3. Fits of the pseudorapidity density with the CKCJ hydro solution,¹⁶ to CMS Xe+Xe data at $\sqrt{s_{NN}} = 5.44$ TeV (Ref. 53) in the 0-80 % centrality class. This fit is obtained by the strongest, Gaussian approximation for the rapidity density, corresponding to Eqs. (24,25,43). The fit parameters are the mean multiplicity $\langle N \rangle$, the Gaussian width of the pseudorapidity distribution Δy and the dimensionless dip parameter D . The fine CKCJ fit quality, the fit range (that includes all the datapoints), and the best value of each of the fitted parameters is indicated on the plot. Yellow band indicates the systematic errors of the CMS measurement. This fit describes the data in a larger pseudorapidity domain than expected, as detailed in the body of the manuscript. We have also evaluated the CKCJ prediction for the rapidity density using the same set of parameters, and overlaid the plot of the rapidity density on that of the pseudorapidity density, corresponding to the same physics but to different measurables.

Table 1. Freeze-out proper-times τ_f extracted from the transverse mass dependent longitudinal HBT radii using Eq. (48) of the CKCJ exact solutions, assuming different values for the freeze-out temperature T_f .

$\sqrt{s_{NN}}$	Au+Au at 130 GeV, 0-30 %		Au+Au at 200 GeV, 0-30 %	
T_f [MeV]	140	175	140	175
τ_f [fm/c]	13.2 ± 0.6	11.8 ± 0.5	11.3 ± 0.4	10.2 ± 0.3

ues i.e. for shorter lifetimes, corresponding to $T_f = 175$ MeV, which value is also consistent with the systematics of the transverse momentum spectra as indicated on Figure 1.

With the help of these values of the lifetime parameter τ_f we are ready to

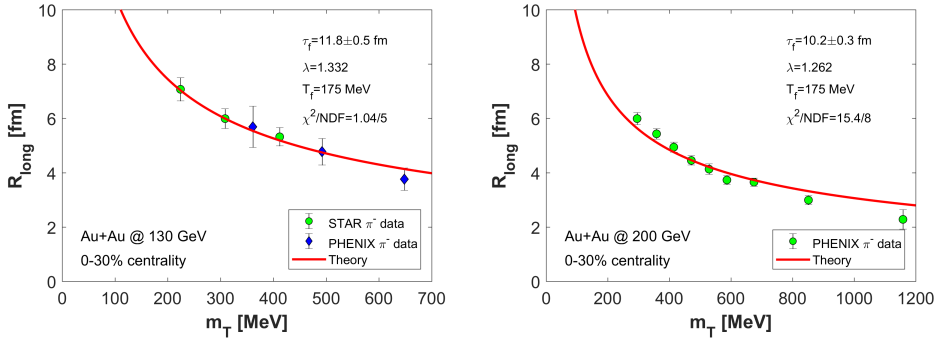
26 *G. Kasza, T. Csörgő*


Figure 4. Fits of the longitudinal HBT-radii with the CKCJ hydro solution,¹⁶ to PHENIX and STAR Au+Au data at $\sqrt{s_{NN}} = 130$ GeV⁴⁵ (left) and to PHENIX Au+Au data at $\sqrt{s_{NN}} = 200$ GeV³⁵ (right) in the 0-30 % centrality class, for a fixed centrality class and colliding system.

calculate the initial energy density of the expanding medium as a function of its initial proper time, τ_0 . This consideration serves the topic of the next section.

5. Initial energy density

In Ref. 18 we have already shown an exact calculation of the initial energy density of the expanding fireball by utilizing the CKCJ hydrodynamic solution. We have found that Bjorken's famous estimate,³ denoted by $\varepsilon_0^{\text{Bj}}$, is corrected by the following formula, if the rapidity distribution is not flat and if the CKCJ solution is a valid approximation for the longitudinal dynamics:

$$\varepsilon_0(\kappa, \lambda) = \varepsilon_0^{\text{Bj}}(2\lambda - 1) \left(\frac{\tau_f}{\tau_0} \right)^{\lambda(1 + \frac{1}{\kappa}) - 1}, \quad (59)$$

where Bjorken's (under)estimate for the initial energy density reads as

$$\varepsilon_0^{\text{Bj}} = \frac{\langle E_T \rangle}{S_\perp \tau_0} \left. \frac{dN}{d\eta_p} \right|_{\eta_p=0}. \quad (60)$$

In Bjorken's estimate S_\perp is the overlap area of the colliding nuclei, and $\langle E_T \rangle$ is the average of the total transverse energy. In Eq. (59) the $(2\lambda - 1)(\tau_f/\tau_0)^{\lambda - 1}$ factor takes into account the shift of the saddle-point corresponding to the point of maximum emittivity for particles with a given rapidity, and it takes into account also the change of the volume element during the non-boost-invariant expansion. In addition to that, we have found an unexpected and in retrospective rather surprising feature of the energy density estimate from the CKCJ solution, as detailed in Ref. 18. Due to the EoS dependent correction factor, in the boost-invariant limit, corresponding to $\lambda = 1$ and to the lack of acceleration, our estimate does *not* reproduce the Bjorken estimate for the initial energy density. However, in this boost-invariant limit the CKCJ result for the initial energy density corresponds to Sinyukov's result from Ref. 46.

This difference between Bjorken's and our estimate for the initial energy density, that exists even in the boost invariant $\lambda = 1$ limit, is related to the work, which is done by the pressure during the expansion stage. If the pressure is vanishing, $p = 0$, it corresponds to the equation of state of dust, and is obtained in the $1/\kappa \rightarrow 0$ limit of our calculations. If $\lambda \rightarrow 1$ and $1/\kappa \rightarrow 0$, our estimate for the initial energy density reproduces Bjorken's estimate.¹⁸ In summary, the Bjorken estimate of the initial energy density has to be corrected not only due to the lack of boost-invariance in the measured rapidity distributions, but also because it neglects that fraction of the initial energy, which is converted to the work done by the pressure during the expansion of the volume element in the center of the fireball.¹⁸ Bjorken was actually aware of this $p = 0$ approximation in his original paper,³ which is a reasonable approximation if $p \ll \varepsilon$ and if one aims to get an order of magnitude estimations, that is precise within a factor of 10. However, at the present age of complex and very expensive accelerators and experiments, an order of magnitude or factor of 10 increase in initial energy density is less, than what can be gained by moving from the RHIC collider top energy of $\sqrt{s_{NN}} = 200$ GeV for Au+Au collisions to the $\sqrt{s_{NN}} = 2.76$ TeV for Pb+Pb collisions at LHC. Although the rise in the center of mass energy is more than a factor of 13 when going from the RHIC energy of $\sqrt{s_{NN}} = 200$ GeV to the LHC energy of $\sqrt{s_{NN}} = 2.76$ TeV, the increase in the initial energy density is of the order of 2 only, as demonstrated recently for example in Ref. 47 and summarized in Table 2. Note that the values of κ -dependent estimates of the initial energy density, $\varepsilon^{\text{conj}}(\kappa, \lambda)$ values of Ref. 47 were based on a conjectured κ dependence of the initial energy density, given in Ref. 48 as follows:

$$\varepsilon_0^{\text{CNC}}(\lambda) = \varepsilon_0^{\text{Bj}}(2\lambda - 1) \left(\frac{\tau_f}{\tau_0} \right)^{\lambda-1}, \quad (61)$$

$$\varepsilon_0^{\text{conj}}(\kappa, \lambda) = \varepsilon_0^{\text{CNC}}(\lambda) \left(\frac{\tau_f}{\tau_0} \right)^{(\lambda-1)(1-\frac{1}{\kappa})}. \quad (62)$$

The first of the above equations is an exact, proper-time dependent result for $\varepsilon_0^{\text{CNC}}(\lambda)$, the initial energy density in the CNC solution of Refs. 30,31,48. However, this Eq. (61) lacks the dependence of the initial energy density on the equation of state parameter κ . Nevertheless it contains two λ -dependent prefactors as compared to the Bjorken estimate, and so it allows for the possibility of a non-monotonic dependence of the initial energy density on the energy of the collision, if the shape and the transverse energy density both change monotonously but non-trivially with $\sqrt{s_{NN}}$.

The second estimate of the initial energy density, Eq. (62) was a conjecture, assumed at times when the CKCJ solution was not yet known. This conjecture was obtained under the condition that it reproduces the exact CNC result in the $\kappa \rightarrow 1$ as well as in the $\lambda \rightarrow 1$ limits.⁴⁸ As compared to the CNC estimate, this conjecture contains a proper-time dependent prefactor, that generalized the CNC estimate under the requirement that it has to reproduce the Bjorken estimate in the $\lambda \rightarrow 1$ limit for all values of the parameter of the Equation of State κ . This is reflected

Table 2. Initial energy density estimation from Ref. 47 by Bjorken's formula $\varepsilon_0^{\text{Bj}}$, and the conjectured values of $\varepsilon_0^{\text{conj}}(\kappa, \lambda)$, evaluated for $\tau_0 = 1$ fm/c. These values also indicate the non-monotonic behaviour of the initial energy density as a function of $\sqrt{s_{NN}}$, the center of mass energy of colliding nucleon pairs.

	$\varepsilon_0^{\text{Bj}}$ [GeV/fm ³]	$\varepsilon_0^{\text{CNC}}(\lambda)$ [GeV/fm ³]	$\varepsilon_0^{\text{conj}}(\kappa, \lambda)$ [GeV/fm ³]	$\varepsilon_0(\kappa, \lambda)$ [GeV/fm ³]
Au+Au at 130 GeV, 6-15 %	4.1 ± 0.4	14.8 ± 2.2	11.2 ± 1.8	11.9 ± 0.5
Au+Au at 200 GeV, 6-15 %	4.7 ± 0.5	12.2 ± 2.3	9.9 ± 1.6	9.8 ± 0.4
Pb+Pb at 2.76 TeV, 10-20 %	10.1 ± 0.3	14.1 ± 0.5	13.3 ± 0.6	

by the vanishing of the exponent of the second proper-time dependent factor in the $\lambda \rightarrow 1$ limiting case. However, by now we know that this requirement is not valid as the initial energy density has a so far largely ignored but also equation of state dependent prefactor. This is due to an actual κ dependent (but neglected) term in the initial energy density in the boost-invariant $\lambda \rightarrow 1$ limiting case. Fortunately the conjecture was numerically reasonably good, as it contained the dominant and fastly rising $(2\lambda - 1)(\tau_f/\tau_0)^{\lambda-1}$ prefactor already, that increases with increasing values of λ that corresponds to decreasing energies and increasing deviations from an asymptotic boost-invariance. Table 2 summarizes the Bjorken, the CNC exact and conjectured initial energy densities, and the CKCJ exact initial densities for $\sqrt{s_{NN}} = 130$ and 200 GeV, 0-30% Au+Au collisions in the first two lines. The last line of the same table also indicates the Bjorken, the CNC and the CNC conjectured result for the initial energy density for $\sqrt{s_{NN}} = 2.76$ TeV Pb+Pb collisions at CERN LHC, assuming the value of $\tau_f/\tau_0 = 10$. The first column of this Table 2 indicates that the Bjorken initial energy density increases monotonically with increasing $\sqrt{s_{NN}}$. The second column indicates that the acceleration parameter λ dependent correction terms generate a *non-monotonic* energy dependence for the initial energy density already in the CNC model fit results. As the evolution of the shape of the pseudorapidity distribution is rather dramatic at lower energies, we can identify that the shape parameter λ dependent terms in Eq. (61) create this *non-monotonic* behaviour, that in turn is inherited by the more-and-more refined calculations, corresponding to the conjecture and to the CKCJ solution indicated in the last two columns of the same Table 2.

Given that a more precise evaluation of the life-time parameter of 2.76 TeV Pb+Pb collisions needs more detailed analysis of this reaction with the help of the CKCJ solution, that goes beyond the scope of our already extended manuscript, the last cell in Table 2 is left empty, to be filled in by future calculations.

Let us use the fit parameters determined in Section 4 to the evaluation of our new, exact result for the initial energy density and for a comparison of it with Bjorken's estimate for the initial energy density, as a function of the initial proper time τ_0 . In Figure 5 we compare Eq. (59) to $\varepsilon_0^{\text{Bj}}$ in Au+Au $\sqrt{s_{NN}} = 130$ GeV and $\sqrt{s_{NN}} = 200$ GeV collisions. The normalization at midrapidity $\left. \frac{dN}{dy} \right|_{y=0}$, the acceleration parameter λ as well as the effective temperature T_{eff} are determined by fits

shown on Figures 1 and 2, while the value of the lifetime parameter τ_f is taken from fits illustrated in Figure 4. The normalization parameter $\left. \frac{dN}{dy} \right|_{y=0}$ corresponds to all the final state particles, and many of them are emitted from the decays of resonances, while the hydrodynamical evolution is restricted to describe the production of directly emitted particles that mix with the short-lived resonance decays whose life-time is comparable to the 1-2 fm/c duration of the freeze-out process. This thermal part of hadron production can be calculated from the exact solutions of relativistic hydrodynamics, but they should be corrected for the contribution of the decays of the long-lived resonances. According to the Core-Halo model,⁴⁹ particle emission is divided into two parts. The Core corresponds to the direct production, which includes the hydrodynamic evolution and the short-lived resonances that decay on the time-scale of the freeze-out process. This part is responsible for the hydrodynamical behavior of the HBT radii and for that of the slopes of the single-particle spectra, a behaviour that is successfully describing the data shown in Figures 1, 4 as well as the shape of the pseudo-rapidity distributions on Fig. 2. On the other hand, the halo part consists of those particles, predominantly pions, that are emitted from the decays of long lived resonances. Exact hydrodynamic solutions, such as the CKCJ solutions can make predictions only for the time evolution of the core. According to the core-halo model of Ref. 49 the normalization parameter of the pseudo-rapidity density, $\left. \frac{dN}{d\eta_p} \right|_{\eta_p=0}$ can be corrected by a measurable core-halo correction factor, to get the contribution of the core from Bose-Einstein correlation measurements:

$$\left. \frac{dN_{\text{core}}}{d\eta_p} \right|_{\eta_p=0} = \sqrt{\lambda_{*}^{\text{HBT}}} \left. \frac{dN}{d\eta_p} \right|_{\eta_p=0}, \quad (63)$$

where the newly introduced the intercept of the two-pion Bose-Einstein correlation function, λ_{*}^{HBT} is taken from measurements of Bose-Einstein correlation functions. In principle this correction factor is transverse mass and pseudorapidity dependent. However, its transverse mass dependence is averaged out in the pseudorapidity distributions so we take its typical value at the average transverse mass, at midrapidity. In addition, the pseudorapidity dependence of this intercept parameter is, as far as we are aware of, not determined in Au+Au collisions at RHIC, given that the STAR and the PHENIX measurements of the Bose-Einstein correlation functions were performed at mid-rapidity, as both detectors identify pions around mid-rapidity only. In the core-halo model, its value is given as $\lambda_{*}^{\text{HBT}} = N_{\text{core}}^2/N^2$ and its average value is measured through the HBT or Bose-Einstein correlation functions for Au+Au $\sqrt{s_{NN}}=130$ GeV (Ref. 45) and $\sqrt{s_{NN}}=200$ GeV (Ref. 35) as well. The size of the overlap area of the colliding nuclei, S_{\perp} is estimated by the Glauber calculations of Ref. 50, and the average thermalized transverse energy is estimated from the nearly exponential shape of the transverse momentum spectra in $m_T - m$ as follows:

$$\langle E_T^{th} \rangle = (m + T_{\text{eff}}) \left(1 + \frac{T_{\text{eff}}^2}{(m + T_{\text{eff}})^2} \right). \quad (64)$$

30 *G. Kasza, T. Csörgő*

This estimate includes only the thermalized energy, which estimate corresponds to the CKCJ solution estimate after being embedded into 1+3 dimensions. Correspondingly, the energy density present in high p_T processes is neglected by this formula and its applications yield a lower limit of the initial energy density. The measured values of the transverse energy production at mid-rapidity, however, include the effects of high transverse momentum processes from perturbative QCD. The difference between the two kind of initial energy densities, the thermalized source and the full initial energy density is illustrated as the difference between the left and the right panels of Figure 6.

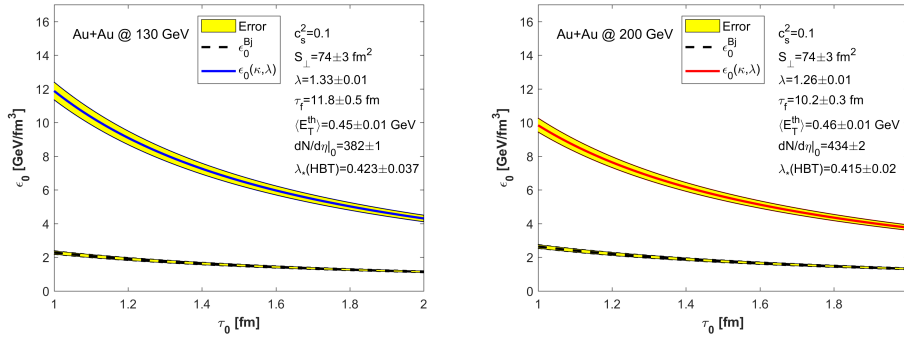


Figure 5. Initial energy density estimates from the CKCJ solution are shown with solid lines and compared to Bjorken's estimate, indicated with dashed lines, as a function of the initial proper time. The parameters of the left panel correspond to fit results of the CKCJ solution to PHOBOS Au+Au pseudorapidity density data in the 0-30 % centrality class both at $\sqrt{s_{NN}} = 130$ GeV (left panel) at $\sqrt{s_{NN}} = 200$ GeV (right panel).

Figure 5 indicates, that Bjorken's formula underpredicts the initial energy density for both collision energies and that it predicts higher initial energy densities for higher collision energies, because the pseudorapidity density of the average transverse energy, $d\langle E_T \rangle / d\eta_p$ is a monotonously increasing function of the colliding energy $\sqrt{s_{NN}}$ for a given centrality class. However, an unexpected and really surprising feature is also visible on these plots: namely, our formula finds that for the lower collision energies of $\sqrt{s_{NN}} = 130$ GeV, the initial energy densities are higher, due to the larger acceleration and work effects, than at the larger colliding energies of $\sqrt{s_{NN}} = 200$ GeV! This unexpected behaviour is caused by an interplay of two different effects. Although the midrapidity density is increasing monotonically with increasing colliding energy, that would increase the initial energy densities with increasing energy of the collision, the acceleration and the related work effects decrease with increasing energies. Although both $\frac{dE}{d\eta_p}|_{\eta_p=0}$ and λ change as a monotonic function of $\sqrt{s_{NN}}$, ε_0 is a non-trivial function of both λ and $\frac{dE}{d\eta_p}|_{\eta_p=0}$, so that the net effect is a decrease of the initial energy density with increasing colliding energies. Thus the CKCJ corrections of the Bjorken estimation have more significant effects in

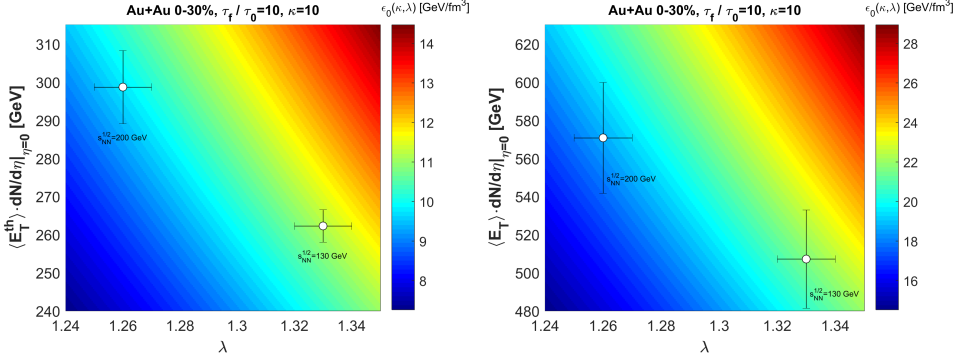


Figure 6. Location of the 0-30 % central Au+Au collisions on the $(\lambda, dE_T/d\eta_p)$ diagram for $\sqrt{s} = 130$ and 200 GeV. The color code indicates the contours of constant initial energy densities, evaluated for the realistic $\kappa = 10$ equation of state, corresponding to the measured speed of sound $c_s^2 \simeq 0.1$ in these reactions. Conservatively, these contours are evaluated for a $\tau_f/\tau_0 = 10$ ratio of the final over initial proper-time. The left panel indicates the thermalized energy density while the right panel indicates the pseudorapidity density of all transverse energy, including energy in non-thermal, high transverse momentum processes.

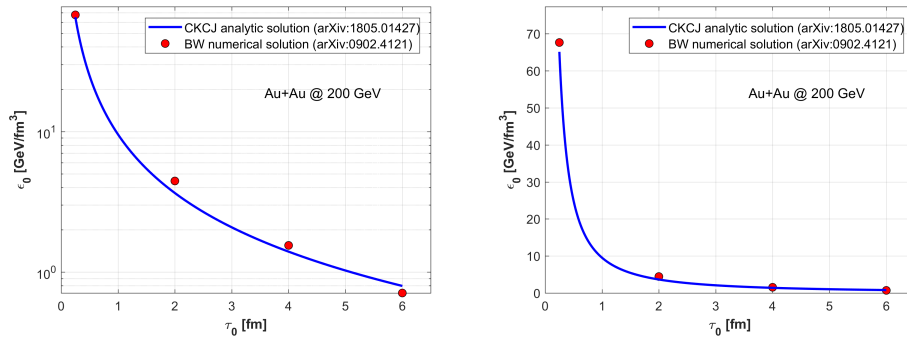


Figure 7. Initial energy density estimates from CKCJ analytic solution are show with blue solid lines and compared to the initial energy estimate from a numerical calculation of Bozek and Wyskiel,⁵¹ indicated with red markers, as a function of the initial proper time. These (blue) solid curves correspond to the (red) solid curves of the right panel Fig. 5 . The left panel shows the same plot as the right panel, but the left panel uses a logarithmic vertical scale for a comparison of the (red) markers with the (blue) solid line, while the right panel uses a linear vertical scale to show the same comparison.

lower collision energy because of the greater acceleration and longer lifetime of the fireball.

This feature is clearly illustrated on both the left and the right panels of Fig. 6. The projection of the two data points to the vertical axis indicates that the transverse energy production is a monotonically increasing function with increasing $\sqrt{s_{NN}}$ for Au+Au collisions in the same centrality class. This feature is independent of the usage of the thermalized energy density (left panel) or the total available en-

ergy density (right panel). The projection of the two points to the horizontal axis is also indicating a monotonously changing/flattening shape of the (pseudo)rapidity distribution with increasing $\sqrt{s_{NN}}$. However, the contours of constant initial density are non-trivially dependent on both the vertical and the horizontal axes, and the location of the two points on the two-dimensional plot with respect to the contour lines indicates, that the initial energy density in $\sqrt{s_{NN}} = 200$ GeV Au+Au collisions is actually less than the initial energy density in the same reactions but at lower, 130 GeV colliding energies, in the same 0-30 % centrality class.

The astute reader may think at this point that such a non-monotonic behaviour of the initial energy density as a function of the colliding energy may be due just to the 1+1 dimensional nature of the adopted CKCJ solution i.e. the neglect of the effects of transverse expansion on the transverse energy density and also due to the neglect of a possible temperature dependence of the speed of sound.

To cross-check and clarify these questions, in Fig. 7 we compared the CKCJ initial energy density estimate of Au+Au collisions at $\sqrt{s_{NN}}=200$ GeV in the 0-30% centrality class to the 1+3 dimensional numerical solution of the equations of relativistic hydrodynamics by Bozek and Wyslkiel (BW).⁵¹ This numerical result was shown to reproduce the pseudorapidity density of charged particles in $\sqrt{s_{NN}} = 200$ GeV Au+Au collisions, using lattice QCD equation of state, with a temperature dependent speed of sound. Both of the analytic and numerical estimations are corrected for the decays of (long-lived) resonances, so Fig. 7 compares only the thermalized initial energy densities from the CKCJ analytic solution and from the BW numerical solution. The estimation of the analytic but 1+1 dimensional CKCJ solution is surprisingly similar to the numerical but 1 + 3 dimensional calculations as far as initial energy densities are concerned. The similarity of the evolution of the energy density in the center of the fireball in these two different hydrodynamical solutions may just be a coincidence, given that Ref. 51 did not detail the centrality dependence of the time evolution of the energy density. However, the centrality dependence is expected to influence the overall normalization predominantly, so the similar time-dependence of the decrease of the energy density in the CKCJ solution and in the calculations of Ref. 51 clearly indicates, that the collective dynamics in the center of the fireball is predominantly longitudinal and that transverse flow effects do not substantially modify the pseudorapidity density of transverse energy at mid-rapidity – as conjectured by Bjorken in Ref. 3.

Although the centrality classes and the estimations of the EoS dependence of the initial energy densities are somewhat different in the current work as compared to that of Ref. 47, that paper provides an additional possibility for a cross-check. The results are summarized in Table 2. It is important to realize, that in Ref. 47 the critical energy densities as well as their non-monotonic dependence on $\sqrt{s_{NN}}$ are within errors the same as in the exact calculations presented in this paper, that can be seen from a comparison of the last two columns of Table 2, where the results in the last column correspond to Fig. 5.

6. Summary

In this manuscript, we started to evaluate the excitation functions of the main characteristics of high energy heavy ion collisions in the RHIC energy range. The initial energy density and the lifetime of these reactions was estimated with the help of a novel family of exact and analytic, finite and accelerating, 1+1 dimensional solutions of relativistic perfect fluid hydrodynamics, found recently by Csörgő, Kasza, Csanád and Jiang.¹⁶ With this new solution we evaluated the rapidity and the pseudorapidity densities and demonstrated, that these results describe well the pseudorapidity densities of Au+Au collisions at $\sqrt{s_{NN}} = 130$ GeV and $\sqrt{s_{NN}} = 200$ GeV in the 0-30% centrality class.

We have obtained three remarkable theoretical results:

- We have derived a simple and beautiful formula to describe the pseudorapidity density distribution from the CKCJ solution of relativistic hydrodynamics.¹⁶ This formula is given by Eqs. (42) and (43), and it describes not only $p+p$ and heavy ion data at RHIC and LHC energies, but it also describes the recent CMS data on Xe + Xe collisions exceedingly well.
- We have derived the scaling relation that at mid-rapidity, $R_{\text{long}} = A \left(\frac{dN}{dn_p} \right)^{1/3}$ follows from the CKCJ solution of relativistic hydrodynamics¹⁶. This scaling relation has been discovered empirically in Ref. 37 and this relation has been found to be valid for a broad set of data in a recent paper by the ALICE collaboration in Ref. 33, but, as far as we know, this relation has not been derived from relativistic hydrodynamics before.
- We have found a new method to extract the initial energy density of high energy proton-proton and heavy ion collisions, that corrects Bjorken's initial energy density estimate for realistic pseudo-rapidity density distributions.

From fits to these pseudorapidity distributions, we determined the acceleration parameter λ as well as the effective temperature, the slope of the transverse momentum distribution T_{eff} . With the help of these values, we reduced the number of free fit parameters to one in the analytic expression from the CKCJ solution that describes the transverse mass dependence of the longitudinal HBT-radii. We have determined the freeze-out proper time τ_f from transverse mass dependent fits to PHENIX and STAR R_{long} measurements. We have found that $\tau_f = 11.8 \pm 0.5$ fm at $\sqrt{s_{NN}} = 130$ GeV and $\tau_f = 10.2 \pm 0.3$ fm at $\sqrt{s_{NN}} = 200$ GeV Au+Au collisions in the 0-30 % centrality class. These values were utilized to evaluate the initial energy densities, as a function of the initial proper time, for both collision systems. We compared our new, exactly calculated formula to Bjorken's estimate and the results were quite surprising. The CKCJ solution and the corresponding data analysis finds higher initial energy densities in $\sqrt{s_{NN}} = 130$ GeV Au+Au collisions in the 0-30 % centrality class as compared to the same kind of collisions at larger, $\sqrt{s_{NN}} = 200$ GeV colliding energies.

- The applications of our results to Au + Au data at RHIC and Pb+Pb collisions at LHC energies suggest, that the initial energy density is a non-monotonic function of the colliding energy at the RHIC energy range of $\sqrt{s_{NN}} \leq 200$ GeV, given that at the LHC energies the initial energy densities increase, as indicated on Table 2.

We find that the observed decrease of the initial energy density from $\sqrt{s_{NN}} = 130$ GeV to 200 GeV collisions is an indication of a non-monotonic behaviour, that has a limited range, as the initial energy density increases from $\sqrt{s_{NN}} = 200$ GeV to $\sqrt{s_{NN}} = 2.76$ TeV heavy ion collisions. It is thus important and urgent to map out the dependence of the initial energy density of high energy heavy ion collisions on the colliding energy for all currently available data sets.

Let us comment on the counterintuitive behavior of the initial temperature. Its dropping with center of mass energy increasing from $\sqrt{s_{NN}}$ growing from 130 to 200 GeV apparently contradicts basic QCD-related ideas on the physics of multi-particle production, as the gluon density is expected to increase monotonically with increasing colliding energy. However, near the QCD critical point, several physical quantities like the initial conditions as well as final state observables are expected to behave non-monotonically. The detailed evaluation of the excitation function of the initial energy density as proposed in our manuscript may thus also become a new tool to search for the critical point of the QCD phase diagram: in the vicinity of this critical point, several quantities may behave in a non-monotonic manner, including life-time related observables. For example, the non-monotonic behaviour of the HBT-radii has been observed in the RHIC energy domain, pointing to a QCD critical point near $\mu_B \approx 95$ MeV, corresponding to $\sqrt{s_{NN}} \approx 47.5$ GeV.⁵² Our data analysis related to the estimations of the initial energy density of *Au + Au* collisions at RHIC supports independently the possibility of such a scenario, although more detailed studies at lower RHIC energies and a refined treatment of the forward and backward rapidity regions are needed to try to locate the QCD critical point with our method. Based on these arguments we may expect that the initial energy density increases monotonically with increasing colliding energy, then in a limited range of colliding energies it may decrease with further increase (eg. from $\sqrt{s_{NN}} \geq 47.5$ GeV up to 200 GeV). However, at higher colliding energies, where the gluons dominate totally the initial energy density, the initial temperatures and energy densities may become again monotonically increasing functions of the colliding energy.

In order to refine our resolution of our "femtoscope" further, and in order to deepen our understanding, the generalizations of the CKCJ solution to the cases of *i*) a temperature dependent speed of sound, *ii*) a one plus three dimensional expansion, *iii*) viscous solutions with shear and bulk viscosity terms are being explored at the time of closing this manuscript.

Acknowledgments

We would like to thank M. Csanád, L. Lönnblad, R. Pasechnik, G. Gustafson and J. Schukraft for clarifying, inspiring and useful discussions. T. Cs. expresses his gratitude to R. Pasechnik for inviting the presentation of these results to the COST Workshop on the Interplay of Hard and Soft QCD Probes for Collectivity in Heavy Ion Collisions and for a kind hospitality at the University of Lund. It is our pleasure to thank one of the Referees of IJMPA for his or her insights and constructive criticism during the anonymous peer-review process. Our research has been partially supported by the THOR project, COST Action CA15213 of the European Union, as well as by the Hungarian NKIFH grants FK-123842 and FK-123959 and the EFOP-3.6.1-16-2016-00001 grants (Hungary).

Bibliography

1. E. Fermi, *Prog. Theor. Phys.* **5**, 570 (1950).
2. L. D. Landau, *Izv. Akad. Nauk Ser. Fiz.* **17**, 51 (1953).
3. J. D. Bjorken, *Phys. Rev. D* **27**, 140 (1983).
4. N. M. Agababyan *et al.* [EHS/NA22 Collaboration], *Phys. Lett. B* **422**, 359 (1998) [hep-ex/9711009].
5. I. Arsene *et al.* [BRAHMS Collaboration], *Nucl. Phys. A* **757**, 1 (2005) [nucl-ex/0410020].
6. K. Adcox *et al.* [PHENIX Collaboration], *Nucl. Phys. A* **757**, 184 (2005) [nucl-ex/0410003].
7. B. B. Back *et al.*, [PHOBOS Collaboration], *Nucl. Phys. A* **757**, 28 (2005) [nucl-ex/0410022].
8. J. Adams *et al.* [STAR Collaboration], *Nucl. Phys. A* **757**, 102 (2005) [nucl-ex/0501009].
9. L. Adamczyk *et al.* [STAR Collaboration], *Nature* **548**, 62 (2017) [arXiv:1701.06657 [nucl-ex]].
10. C. Aidala *et al.* [PHENIX Collaboration], *Nature Phys.* **15**, no. 3, 214 (2019) [arXiv:1805.02973 [nucl-ex]].
11. C. Aidala *et al.* [PHENIX Collaboration], *Phys. Rev. Lett.* **120**, no. 6, 062302 (2018) [arXiv:1707.06108 [nucl-ex]].
12. J. L. Nagle and W. A. Zajc, *Ann. Rev. Nucl. Part. Sci.* **68**, 211 (2018) [arXiv:1801.03477 [nucl-ex]].
13. J. Adam *et al.* [ALICE Collaboration], *Nature Phys.* **13**, 535 (2017) [arXiv:1606.07424 [nucl-ex]].
14. F. Nemes, T. Csörgő and M. Csanád, *Int. J. Mod. Phys. A* **30**, no. 14, 1550076 (2015) [arXiv:1505.01415 [hep-ph]].
15. R. Derradi de Souza, T. Koide and T. Kodama, *Prog. Part. Nucl. Phys.* **86**, 35 (2016) [arXiv:1506.03863 [nucl-th]].
16. T. Csörgő, G. Kasza, M. Csanád and Z. Jiang, *Universe* **4** (2018) 69 [arXiv:1805.01427 [nucl-th]].
17. T. Csörgő, G. Kasza, M. Csanád and Z. F. Jiang, *Acta Physica Polonica B* **50** (2019) p. 27 arXiv:1806.06794 [nucl-th].
18. G. Kasza and T. Csörgő, *Acta Physica Polonica B Proceedings Supplement v. 12* (2019) p. 175 arXiv:1806.11309 [nucl-th].
19. T. Csörgő and G. Kasza, *Acta Physica Polonica B Proceedings Supplement v. 12*

36 *G. Kasza, T. Csörgő*

- (2019) p. 217 arXiv:1810.00154 [nucl-th].
20. T. Csörgő, S. V. Akkelin, Y. Hama, B. Lukács and Y. M. Sinyukov, Phys. Rev. C **67**, 034904 (2003) [hep-ph/0108067].
 21. M. Csanád, M. I. Nagy and S. Lökös, Eur. Phys. J. A **48**, 173 (2012) [arXiv:1205.5965 [nucl-th]].
 22. T. Csörgő and M. I. Nagy, Phys. Rev. C **89** (2014) no.4, 044901 [arXiv:1309.4390 [nucl-th]].
 23. T. Csörgő and G. Kasza, JCEGI 5:(2) pp. 19-32. (2016) [arXiv:1610.02197 [nucl-th]].
 24. A. Adare *et al.* [PHENIX Collaboration], Phys. Rev. Lett. **98**, 162301 (2007) [nucl-ex/0608033].
 25. S. Borsányi, G. Endrődi, Z. Fodor, A. Jakovác, S. D. Katz, S. Krieg, C. Ratti and K. K. Szabó, JHEP **1011**, 077 (2010) [arXiv:1007.2580 [hep-lat]].
 26. B. Alver *et al.* [PHOBOS Collaboration], Phys. Rev. C **83**, 024913 (2011) [arXiv:1011.1940 [nucl-ex]].
 27. T. Csörgő and B. Lörstad, Phys. Rev. C **54**, 1390 (1996)
 28. M. I. Nagy and T. Csörgő, Phys. Rev. C **94**, no. 6, 064906 (2016) [arXiv:1606.09160 [hep-ph]].
 29. M. I. Nagy, Phys. Rev. C **83**, 054901 (2011) [arXiv:0909.4285 [nucl-th]].
 30. T. Csörgő, M. I. Nagy and M. Csanád, Phys. Lett. B **663**, 306 (2008) [nucl-th/0605070].
 31. M. I. Nagy, T. Csörgő and M. Csanád, Phys. Rev. C **77**, 024908 (2008)
 32. A. N. Makhlin and Y. M. Sinyukov, Z. Phys. C **39** (1988) 69.
 33. J. Adam *et al.* [ALICE Collaboration], Phys. Rev. C **91** (2015) 034906 [arXiv:1502.00559 [nucl-ex]].
 34. J. Adams *et al.* [STAR Collaboration], Phys. Rev. C **71**, 044906 (2005) [nucl-ex/0411036].
 35. S. S. Adler *et al.* [PHENIX Collaboration], Phys. Rev. Lett. **93** (2004) 152302 [nucl-ex/0401003].
 36. D. Adamová *et al.* [CERES Collaboration], Nucl. Phys. A **714**, 124 (2003) [nucl-ex/0207005].
 37. M. A. Lisa, S. Pratt, R. Soltz and U. Wiedemann, Ann. Rev. Nucl. Part. Sci. **55**, 357 (2005) [nucl-ex/0505014].
 38. R. C. Hwa, Phys. Rev. D **10** (1974) 2260.
 39. P. Cszimadia, T. Csörgő and B. Lukács, Phys. Lett. B **443** (1998) 21 [nucl-th/9805006].
 40. T. Csörgő, Central Eur. J. Phys. **2** (2004) 556 [nucl-th/9809011].
 41. T. Csörgő, M. I. Nagy and I. F. Barna, Phys. Rev. C **93** (2016) no.2, 024916 [arXiv:1511.02593 [nucl-th]].
 42. T. Csörgő and G. Kasza, Universe **4** (2018) no.4, 58 [arXiv:1801.05716 [nucl-th]].
 43. K. Adcox *et al.* [PHENIX Collaboration], Phys. Rev. C **69** (2004) 024904 [nucl-ex/0307010].
 44. S. S. Adler *et al.* [PHENIX Collaboration], Phys. Rev. C **69** (2004) 034909 [nucl-ex/0307022].
 45. K. Adcox *et al.* [PHENIX Collaboration], Phys. Rev. Lett. **88** (2002) 192302 [nucl-ex/0201008].
 46. M. I. Gorenstein, Y. M. Sinyukov and V. I. Zhdanov, Phys. Lett. **71B** (1977) 199.
 47. Z.-F. Jiang, C.-B. Yang, M. Csanád and T. Csörgő, Phys. Rev. C **97** (2018) no.6, 064906 [arXiv:1711.10740 [nucl-th]].
 48. T. Csörgő, M. I. Nagy and M. Csanád, J. Phys. G **35**, 104128 (2008) [arXiv:0805.1562 [nucl-th]].
 49. T. Csörgő, B. Lörstad and J. Zimányi, Z. Phys. C **71** (1996) 491 [hep-ph/9411307].

50. M. L. Miller, K. Reygers, S. J. Sanders and P. Steinberg, *Ann. Rev. Nucl. Part. Sci.* **57** (2007) 205 [nucl-ex/0701025].
51. P. Bozek and I. Wyskiel, *Phys. Rev. C* **79** (2009) 044916 [arXiv:0902.4121 [nucl-th]].
52. R. A. Lacey, *Phys. Rev. Lett.* **114**, no. 14, 142301 (2015) [arXiv:1411.7931 [nucl-ex]].
53. A. M. Sirunyan *et al.* [CMS Collaboration], arXiv:1902.03603 [hep-ex].
54. K. Werner, F. M. Liu and T. Pierog, *Phys. Rev. C* **74** (2006) 044902 [hep-ph/0506232].
55. T. Pierog, I. Karpenko, J. M. Katzy, E. Yatsenko and K. Werner, *Phys. Rev. C* **92** (2015) no.3, 034906 [arXiv:1306.0121 [hep-ph]].
56. I. P. Lokhtin and A. M. Snigirev, *Eur. Phys. J. C* **45** (2006) 211 [hep-ph/0506189].
57. Z. W. Lin, C. M. Ko, B. A. Li, B. Zhang and S. Pal, *Phys. Rev. C* **72** (2005) 064901 [nucl-th/0411110].